MTLA 38 (2024) 102240

Contents lists available at ScienceDirect

Materialia

journal homepage: www.elsevier.com/locate/mtla

Bone regeneration in rabbit cranial defects: 3D printed polylactic acid scaffolds gradually enriched with marine bioderived calcium phosphate

Iván Alonso Fernández [a,*], Håvard Jostein Haugen [b], Liebert Parreiras Nogueira [b],
Miriam López Álvarez [c,d], Pío González [c,d], Mónica López Peña [a],
Antonio González Cantalapiedra [a], Fernando Muñoz Guzón [a]

[a] *Anatomy, Animal Production and Veterinary Clinical Sciences Department, Veterinary Faculty, Universidade de Santiago de Compostela, Campus Universitario s/n, 27002, Lugo, Spain*
[b] *Department of Biomaterials, Institute of Clinical Dentistry, Faculty of Dentistry, University of Oslo, Oslo, Norway*
[c] *CINTECX, Universidade de Vigo, Grupo de Novos Materiais, 36310, Vigo, Spain*
[d] *Galicia Sur Health Research Institute (IIS Galicia Sur), SERGAS-UVIGO, 36213, Vigo, Spain*

ARTICLE INFO

Keywords:
Polylactic acid
Bioceramic
3D-printing technology
Composite scaffolds
Bone regeneration
Rabbit calvarial defect model

ABSTRACT

Objective: This study aimed to evaluate the in vivo biocompatibility, mechanical performance and osteoconductive potential of 3D-printed polylactic acid (PLA) scaffolds enriched with marine bioderived calcium phosphate (bioCaP) for bone tissue engineering.
Materials and methods: PLA-bioCaP composite scaffolds were specifically designed for the rabbit cranial defect model by 3D printing, with a uniform distribution of open square-shaped pores and contributions in bioCaP. Physicochemical and mechanical characterization and the evaluation of biological response are presented.
Results: The scaffolds demonstrated mechanical properties comparable to human bones, integration with the host bone, and osteoconductive behavior promoting cell ingrowth from the defect edge. Strong mineralized tissue ingrowth through the scaffolds' pores was observed, providing notable support to the host bone. In quantitative terms, micro-CT and histomorphometry analysis post-implantation revealed no significant differences in bone regeneration across all groups.
Conclusion: The 3D-printed scaffolds with perpendicular patterning, open porosity, and proposed composition displayed satisfactory mechanical properties, biocompatibility, and osteoconductive response. The scaffolds promoted bone regeneration at similar levels as the PLA. The highest contribution of bioCaP promoted a positive influence in certain histomorphometric parameters; however, it did not significantly improve their osteogenic capability. Further research is required to optimize scaffold composition and enhance their osteogenic potential.
Clinical relevance: This study presents a significant advancement in bone tissue engineering through the development of personalized composite scaffolds for bone-related applications. The clinical implications of this research are profound, especially considering the increasing demand for functional bone regeneration technologies capable of producing cost-effective producing cost-effective customized scaffolds.

1. Introduction

Restoring damaged tissue represents one of the main goals of contemporary medical research [1]. A prolonged life expectancy and an aging world population are originating an increase in bone-related treatments and costs [2,3]. Musculoskeletal pathologies, such as fractures, bone infections or tumors, congenital etiologies, maxillofacial pathologies, or rheumatic diseases, are the most common tissue damages [2–4]. This represents major clinical and socioeconomic problems, resulting in detrimental effects on patients' quality of life and society.

Treating skeletal defects remains a challenging part of many reconstructive surgeries [2,5]. Bone healing is a complex physiological

---

* Corresponding author at: Campus Universitario s/n, 27002 Lugo, Spain.

E-mail addresses: i.alonso.fernandez@usc.es (I.A. Fernández), h.j.haugen@odont.uio.no (H.J. Haugen), l.p.nogueira@odont.uio.no (L.P. Nogueira), miriammsd@uvigo.gal (M.L. Álvarez), pglez@uvigo.gal (P. González), monica.lopez@usc.es (M.L. Peña), antonio.cantalapiedra@usc.es (A.G. Cantalapiedra), fernandom.munoz@usc.es (F.M. Guzón).

https://doi.org/10.1016/j.mtla.2024.102240
Received 12 December 2023; Accepted 20 September 2024

process that can be delayed or impaired for several reasons, such as the type or extent of the injury, the patient's age or gender, an unfavorable wound environment, etc. [2,6,7]. Indeed, bone is the second most transplanted tissue after blood [8].

Bone tissue engineering aims to create clinically relevant bone grafts, focusing on methods to synthesize and/or regenerate bone to restore, maintain, or improve its functions in vivo [3,9]. Autografts are the current "gold standard" bone grafts for bone regeneration, offering all the properties required for a bone graft. The risk of donor-site morbidity, deformity, chronic pain, infection, dysesthesia, scarring, or blood loss greatly limits their use [8,10–12]. Likewise, allografts and xenografts were postulated as possible alternatives. Nevertheless, the immunological response, the lack of osteogenic capacity, and the risk of infectious disease transmission represented several drawbacks that could not be addressed [8,10,11,13]. Thus, the absence of market-available options matching the ideal properties of a bone graft gives rise to the demand for developing higher-performance biomaterials for bone tissue engineering [8,14]. The main objective is to synthesize a material, or a combination of several, that closely mimics the immunological, functional, structural, and mechanical characteristics of the native bone [1].

Scaffold-based approaches were developed to overcome the limitations of powder-type bone grafts, whose low stability, vulnerability to external force, and risk of collapse resulted in undesirable outcomes [15,16]. Scaffolds comprise a three-dimensional solid support structure with an interconnected pore network that must support bone cells, colonization, proliferation, differentiation, and migration [2,3]. Porous structures should allow the diffusion of nutrients, oxygen, growth factors, waste product exchange, capillary infiltration, cell proliferation, and new bone ingrowth from the periphery to the inner part of the scaffold. Regarding an ideal scaffold for bone tissue engineering, some essential issues are architecture, mechanical properties, degradation rate, and osteogenic ability [14,17,18]. Furthermore, it should be sterilizable and reproducible using cost-effective processes [2].

Additive manufacturing (AM) techniques have been demonstrated to satisfy the increasing demand for customizable bone substitutes for bone regeneration by creating 3D-printed porous scaffolds that can be adapted to a patient's specific geometry [19,20]. The fabrication of personalized-shaped scaffolds with precise control of matrix architecture overcomes the limitations of conventional techniques and enhances the control over mechanical properties, biological effects, and degradation kinetics, improving the scaffold's biocompatibility by avoiding organic solvents. [2,18,21].

Selecting adequate biomaterials for scaffold synthesis is a critical step for the success of a bone graft. There is an increasing demand for developing printable, higher-performance biomaterials. Some polymers, ceramics, metals, and self-assembly peptides have been widely studied over the last few years for bone tissue engineering applications [3,14,22].

Polylactic acid (PLA) is a US Food and Drug Administration (FDA) approved biopolymer, which has gained attention for its use in biomedical applications using AM techniques, owing to its biocompatibility, processability, mechanical properties, biodegradability, and absence of toxic or carcinogenic effects. Nevertheless, its slow degradation rate, hydrophobicity, and low cell affinity, as well as the release of acidic degradation by-products that may lead to the appearance of an inflammatory response, represent several drawbacks that need to be addressed to promote the bone healing process [13,15,20,23,24].

Composite materials could be fabricated to overcome PLA limitations by combining the polymeric material with bioactive ceramic particles. Bioceramic materials exhibit effective and safe properties for promoting bone reconstruction and remodeling because of their similarities to natural bone [8,25]. Calcium phosphates (CaP), calcium sulfates and bioactive glasses are some of the available synthetic bone substitutes. Among them, CaP, such as hydroxyapatite (HA) and beta-tricalcium phosphate (β-TCP), are commonly used as bone grafting materials since the primary inorganic component of bone is calcium hydroxyapatite [8,26]. CaP bioceramics are characterized by their biocompatibility and bioactivity because of their abundance in the body and the partial dissolution and release of ionic products that augment the concentration of calcium and phosphate ions. So, they have osteoconductive and even osteoinductive properties, crystal structure, high melting point, and low mechanical characteristics. Their brittle behavior is a critical problem that restricts the broader application of CaP, mainly to non-load-bearing sites [26,27].

Briefly, the development of composite materials generally includes combining a matrix and a reinforcing agent to take advantage of the properties of each one, obtaining a synergistic effect [2,10,26]. PLA has been widely used to synthesize composites with different materials such as hyaluronic acid [15], polycaprolactone (PCL) [28], bioceramic such as HA [29,30] and nano-HA [31,32], bioglasses [30,33], eggshell [34] or β-TCP [35]. Using PLA composite instead of pure PLA polymer was proposed to increase its mechanical strength, biological activity, and osteoconductive properties. It is stated that incorporating CaP bioceramics into PLA filaments satisfy these goals, in addition to reducing the environment's acidification and the inflammatory reactions occasioned by the polymer. The search of new sources of bioderived CaP bioceramics is of great interest nowadays as they usually provide improved biological responses than the synthetic ones, offering more complex biphasic compositions [36]. Thus, developing such a successful PLA composite would expand the use of 3D printing technology in bone tissue engineering [24,37] and have been successfully fabricated and demonstrated to enhance bone formation in vivo [4]. However, a knowledge gap exists regarding the optimal composition and structure. The behavior of bioceramics in the polymeric matrix has a dose-dependent effect, so osteoconductivity and mechanical properties will be directly and inversely proportional to the amount of ceramic material added. Therefore, it is essential to optimally balance CaP's brittleness and PLA's ductility to avoid the loss of the scaffold's bioactivity [4,29,37].

The search for new calcium phosphate ceramics is still required to improve the capacity of the materials for bone regeneration [36,38]. Shark teeth-derived bioapatites (bioCaP) have emerged as an alternative graft material that valorizes Isurus oxyrinchus and Prionace glauca fishing by-products into a higher value-added application [36,39]. Their composition is based on a combination of 65–70%wt apatitic phase (Hydroxyapatite, apatite-(CaF, CaOH) and fluoroapatite), and 25–30%wt non-apatitic phases (tricalcium bis(orthophosphate) and witlockite); together with the presence of trace elements such as F (1.0+−0.5%wt), Na (0.9+−0.2%wt) and Mg (0.65+−0.04%wt) on their apatite-based structure [39]. López-Álvarez et al. (2016) [39] first demonstrated the biocompatibility in vitro of shark teeth-derived bioapatites. Then, the same group performed a pre-clinical trial in rats, comparing those bioapatites with a commercial synthetic biphasic HA/β-TCP (60/40%) bone graft [36]. The results confirmed higher osteointegration and horizontal growth of bone tissue, but also osteoconductive and osteoinductive properties [36]. Likewise, García-González et al. [38] carried out a preliminary clinical trial in dogs and cats with successful results, demonstrating bioapatites as suitable candidates for orthopedic surgery in the veterinary field.

Consequently, adding bioCaP to a PLA matrix is supposed to substantially improve the synthesized scaffolds regarding physical and biological parameters. Varying concentrations of bioCaP in PLA scaffolds will be helpful to further characterize their impact mainly over mechanical properties but also over wettability, surface topography, pore morphology, and porosity, which will be closely related to the in vivo osteoconductive properties of the scaffold. Besides, ions such as F and Mg in the bioCaP will also favor bone regeneration by enhancing the synthesis of cell growth factors and the parathyroid hormone, respectively [39].

Composite PLA-based scaffolds synthesized by 3D printing techniques may compete with autologous bone implants [18]. The present manuscript aims to evaluate the physicochemical and mechanical performance, biocompatibility, and osteoconductive and osteogenic potential of 3D printed PLA-based scaffolds, with a specific patterning and porosity design, gradually enriched with a marine bioderived calcium phosphate using a rabbit calvarial defect model.

2. Materials and methods

2.1. PLA-bioCaP composite synthesis

Commercial polylactic acid pellets (SMARTFIL®, Smart Materials, Jaén, Spain) of 3 mm diameter size were frozen (−80 °C) to facilitate handling and subjected to a milling and sieving process to obtain a reduced diameter size of 80–250 μm, favoring a more homogeneous mixture with the 20–63 μm bioCaP fraction.

The bioderived calcium phosphate was obtained from *Prionace glauca* shark teeth as a fishing byproduct provided by IIM-CSIC (Vigo, Spain), as previously reported [36,39].

Both fractions (PLA and bioCaP) were mixed in different proportions gradually increasing the bioCaP contribution to 1%, 2% and 12% wt. (named as PLA-1CaP, PLA-2CaP, PLA-12CaP) by using a Turbula® 3D mixer (WAB, Nidderau, Germany). Then, the extrusion process (Filastruder, Snellville, Georgia) was performed to obtain filaments from the different mixtures, as already published by Rojas-Lozano et al. [40]. A filament without bioCaP was also produced (PLA).

2.2. Scaffolds fabrication

Each filament was cut into smaller sections and incorporated in a 3D printer (TUMAKER Voladora NX Pellet, Oiartzun, España) to obtain blanking plug-shaped scaffolds with dimensions of 8 mm primary diameter, 6 mm minor diameter, 2 mm height inner section and 1 mm outer one. This 3D-FDM (Fused Deposition Modeling) printer works with a diameter nozzle of 0.8 mm, and the direction of the processing lines perpendicularly alternates from one layer to the overlapped one. Fig. 1 (a–d) shows simulations using Simplify3D Professional Software of the printing process and final scaffold. Samples were packed in a laminar flow cabin and sterilized by a 15 kGy dose of gamma radiation.

2.3. Characterization of the 3D-printed scaffolds

2.3.1. Physicochemical and morphological characterization

Physicochemical characterization of the 3D printed PLA, PLA-1CaP, PLA-2CaP, PLA-12CaP scaffolds was performed by FT-Raman spectroscopy using B&WTEK i-Raman-785S instrument (Metrohm, Herisau, Switzerland) equipped with a BAC 100 Probe (785 nm), to identify the main molecular vibrations corresponding functional groups. Crystalline structure was evaluated by X-ray diffraction (XDR) with a Siemens d-5000 diffractometer (Siemens AG, Munich, Germany), used together with scanning electron microscopy (SEM) micrographs from the top of the scaffolds, obtained with a JEOL JSM-6700 FEG equipment (JEOL Ltd., Tokyo, Japan) operating at an accelerating voltage of 5 kV.

Furthermore, the exposure of 3D-printed scaffolds' surface topography and bioCaP particles was also assessed using a scanning electron microscope (TM3030, Hitachi, Japan), operating at an accelerating voltage of 15 kV.

2.3.2. Pore morphology

Three-dimensional imaging of the scaffolds was obtained using Micro-CT (SkyScan 1172, Bruker-micro-CT, Kontich, Belgium). Scanning parameters were set to 13.54 μm pixels, X-ray source with 70 kV and 141 mA, and using a 0.5 mm Aluminum filter. The raw images of the scaffolds were reconstructed, using the Skyscan standard software (NRecon, Bruker-micro-CT, Kontich, Belgium) to serial coronal-oriented tomograms using a modified back-projection algorithm [41] and subsequently analyzed with another SkyScan software (CTAn, Bruker-micro-CT, Kontich, Belgium). The 3D analysis evaluated

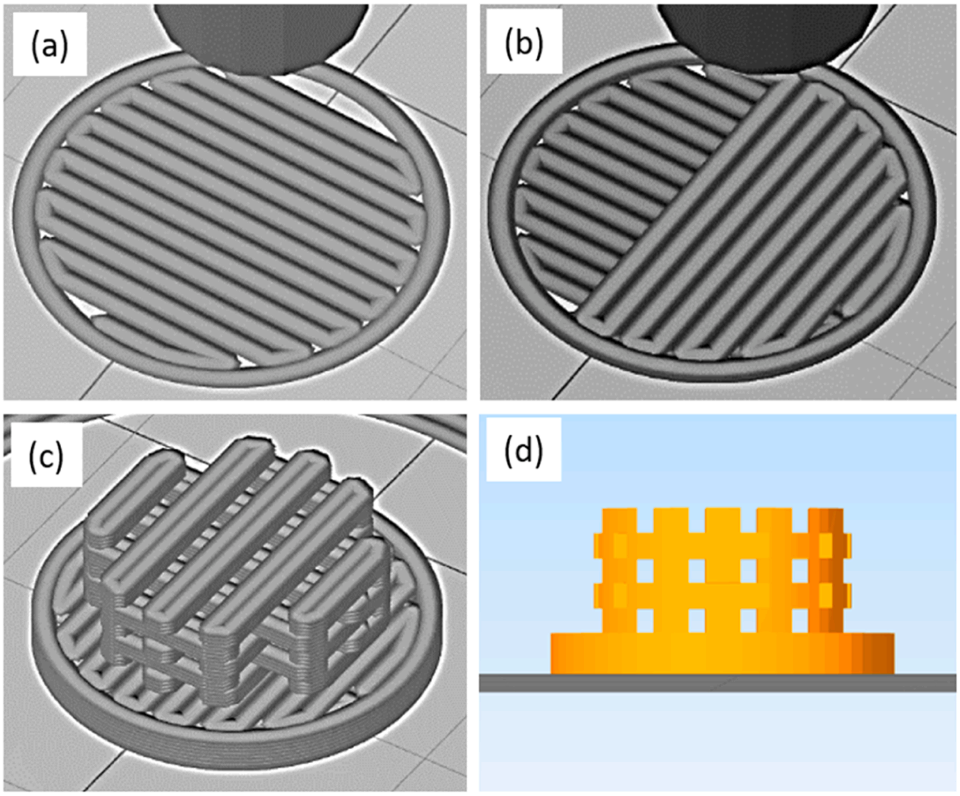

Fig. 1. Sequential illustrations from Simplify3D Professional Software of the 3D printing process (a-c) and final open porosity distribution (d). Scaffolds with 8 mm primary diameter and 1 mm height (tape) and 6 mm minor diameter and 2 mm height in the inner section.

morphological parameters such as open/closed porosity, Strut diameter (Strut Thickness), and pore size. Likewise, interconnectivity was calculated with an algorithm considering only the open and accessible pore volume within the scaffold, as previously described by [42,43]. This method quantifies bone ingrowth as a function of accessible pore size using the invasion radius. It gives the smallest throat, or pore constriction, connecting every voxel to the scaffold periphery [44].

2.3.3. Mechanical test

Compressive mechanical testing (Zwicki, Zwick/Roell, Ulm, Germany) was conducted to evaluate the mechanical strength of the 3D-printed scaffolds. Test Expert II software (Zwick, Germany) was used to calculate the compressive strength based on the scaffold diameter. Compression tests were performed using a load cell of 1 kN. The preloading force was set to be 0.5 N. The standard scaffolds (Φ6 x 2 mm) were compressed along their length axis at a 1 mm/min compression speed until failure. The cross-section area was calculated through microtomographic analysis and established at 13.02 mm^2. The force and displacement were recorded throughout the compression and converted to stress and strain based on the initial scaffold dimensions. The test was performed until the failure of the scaffold, manifested by a plateau region in the compressive stress-strain curve. The compressive strength of the scaffold was considered the maximum stress prior to its failure. It was defined as the maximum stress detected within the linear elasticity phase before reaching the plateau phase and the subsequent densification of collapsed struts as presented in Klemm et al. 2021 [45].

2.3.4. Wettability

The wettability of the scaffolds was determined through a static water contact angle measurement using a goniometer (OCA Plus 20; DataPhysics Instrument GmbH; Germany). Around 1 µl of distilled water was injected onto scaffolds' surface, then images were obtained after droplet formation on scaffolds belonging to different groups ($n = 2$). Finally, the analysis was performed using the Sessile Drop technique in 3 data points for each sample.

2.4. Animal model

Eight healthy adult, skeletally mature male New Zealand White rabbits that these findings were adequately used in this study. The protocol was approved by the Ethics Committee of the University of Santiago de Compostela, and authorized by the Regional Government of Galicia. All animal experiments were conducted in strict adherence to Spanish and European Union Regulation regarding protecting animals used for scientific purposes. This paper was written following the Animals in Research Reporting In Vivo Experiments (ARRIVE) guidelines [46], ensuring the transparency and rigor of our research.

The animal housing and experimental procedures were carried out in the Animal Experimentation Facility of the University of Santiago de Compostela under the supervision of highly experienced and qualified personnel. The animals, after a period of acclimatization, were fed and watered ad libitum and used for the experiment. The expertise of the personnel involved in managing the animals instills confidence in the quality and reliability of the research.

All efforts were made to minimize animal pain and distress perform when performing the surgical procedures. The rabbits were premedicated by administering a combination of medetomidine (50 µg/kg IM, Domtor, Esteve, Barcelona, Spain), ketamine (25 mg/kg IM, Imalgène 1000, Merial, Toulouse, France) and buprenorphine (0.03 mg/kg IM, Buprex, RB Pharmaceuticals, Berkshire, UK) intramuscularly. Using a face mask, general anesthesia was induced and maintained by inhalation anesthesia with isoflurane (Inspiratory Fraction ISO 2.5–4%, Isova-vet, Schering-Plow, Madrid, Spain). In addition, each rabbit received preoperatively enrofloxacin (5 mg/kg SC, Ganadexil 5%, Invesa, Barcelona, Spain) as antibiotic prophylaxis, and meloxicam (0.2 mg/kg SC, Metacam, Boehringer Ingelheim España, Barcelona, Spain) for pain control in addition to the buprenorphine.

Once anesthetized, the rabbits' frontoparietal region were shaved and vigorous disinfection was achieved with a 50/50 mixture of povidone-iodine and alcohol. A longitudinal incision was performed medially in the calvaria along the sagittal line, and the calvarial bone was exposed by elevating a mucoperiosteal flap. Sagital and coronal sutures were identified, outlining left-right parietal and frontal bones. Four separated circular bone defects of 7 mm were created by using a trephine bur (6 mm inner diameter and 7 mm outer diameter) on a surgical handpiece under irrigation with physiologic saline, one on each side of the median and coronal sutures. During the osteotomy, care was taken not to damage the underlying exposed dura mater. Then, the circular bicortical bone segment was luxated by using an osteotome, and the defects were allocated to one of the treatment groups according to block randomization: PLA (control group), PLA-1CaP, PLA-2CaP and PLA-12CaP.

After the implantation of the scaffolds, a simple continuous suture pattern with VICRYL 4/0 (Ethicon, Johnson & Johnson, Madrid, Spain) was used to close subcutaneous tissues, and a simple interrupted suture pattern with the same suture was used to close the skin. Finally, the sedation was reverted with an intramuscular injection of atipamezole (25 ug/kg IM, Nosedorm, Karizoo, Barcelona, Spain). Likewise, the animal received postoperatively for 5 days, enrofloxacin (5 mg/kg, Ganadexil 10%, Invesa, Barcelona, Spain) to avoid infections, and meloxicam (0.1 mg/kg SC, Metacam, Boehringer Ingelheim España, Barcelona, Spain) for pain management. The rabbits were monitored weekly by veterinarians for wound dehiscence, inflammation, infection, and general health until euthanized.

Twelve weeks after the implantation, the animals were sedated with medetomidine (50 ug/kg IM, Domtor, Esteve, Barcelona, Spain) and ketamine (25 mg/kg IM, Imalgène 1000, Merial, Toulouse, France), and then euthanized by sodium pentobarbital (100 mg/kg IV, Dolethal, Vétoquinol, Madrid, Spain) overdose injection in the lateral auricular vein. Immediately after euthanasia, the samples were dissected free of skin and soft tissue, and the calvarial bone was harvested and fixed in 10% buffered formalin for 2 weeks.

2.5. Micro-CT analysis

After the specimens were fixed, they were wrapped in gauze moistened with 10% buffered formalin and scanned before being processed for histology.

The samples were scanned using a high-resolution micro-computed tomography (µCT) machine (Skyscan 1172, Bruker microCT NV, Kontich, Belgium), equipped with an 11-Mpixel CCD camera. The acquisition parameters were set to 70 kV, 141 uA, and an aluminum filter of 0.5 mm. The reconstruction of the X-ray projections was performed using a modified back-projection algorithm [41] (NRecon v.1.7.5, Bruker, Kontich, Belgium) with a final voxel size of 13.58 um. The newly formed bone was analyzed using a CT Analyser (CTAn 1.20.3.0+, Bruker, Kontich, Belgium). Grey-scale values were set from 80 to 255 (0:black; 255:white) for the segmentation of new bone [47]. 3D analysis was performed to evaluate the bone regeneration capabilities of the scaffolds, and the following 3D morphometric quantifications were assessed: Bone Volume/Tissue Volume (BV/TV), Bone Surface/Bone Volume (BS/BV), Trabecular Thickness (Tb.Th.) and Trabecular Pattern Factor (Tb.Pf.).

2.6. Histologic and histomorphometric analysis

Once the specimens were scanned, they were left in 10% buffered formalin for one more week. After that, they were carefully cut along the sagittal and coronal sutures, and the four defects filled with implants performed in each animal were individualized for the next step. They were processed for undecalcified ground sections according to the method described by Donath [48], and cross-sections were generated with a thickness of ~40 µm. Then, tissue slides were stained with Lévai-Laczkó's protocol, and two blinded evaluators carried out a semiquantitative histological evaluation and histomorphometric analysis.

Firstly, all the samples were microscopically (Olympus BX41 microscope; Olympus Corporation, Tokyo, Japan) evaluated according to UNE-EN ISO 10993-6:2017 standard to assess the local effects after scaffolds' implantation. A description of the most notable histological findings was also performed.

For quantitative analyses, the slides were imaged with an Olympus BX51 motorized microscope (Olympus Corporation, Tokyo, Japan). Whole section images were captured at x10 augments, colored with Adobe Photoshop CS6 (Adobe Systems Incorporated, San Jose, USA), and then analyzed to measure the selected histomorphometric parameters using the Olympus CellSens 1.5 (Olympus Corporation). The following measurements were assessed: Bone-to-implant contact (BIC), Implant Surface/Tissue Surface (IS/TS), and Bone Surface/Tissue Surface (BS/TS).

2.7. Statistical analysis

Data were expressed as means ± standard deviations (SDs). The statistical analysis was performed with SigmaPlot 12.5 software for Windows (Systat Software inc., Chicago, IL, USA). The normality of the variables was assessed using the Shapiro-Wilk test, and Levene's test was used to check the equality of variances of normal variables. The statistical comparison of different data groups was performed through a one-way analysis of variance (one-way ANOVA), followed by a post-hoc test for pairwise multiple comparisons (Holm-Sidak method). For non-normal variables, a Friedman One-Way Repeated Measure Analysis of Variance Ranks was performed to evaluate the statistical comparison, and then a post-hoc analysis using the Tuckey Test. In addition, correlation studies were performed by using Pearson's correlation analysis. The statistical significance level was set at $p < 0.05$ for all parameters.

3. Results

3.1. PLA:bioCaP scaffolds characterization

3.1.1. Physicochemical and morphological characterization

The morphology of the 3D printed blanking plug-shaped scaffolds can be observed in Fig. 2 by optical images of PLA-0CaP and PLA-12CaP scaffolds, both with the central region amplified to observe the porosity in more detail and by SEM micrographs from the top of the PLA-12CaP scaffold.

The blanking plug shape of the scaffolds is observed in the optical images (a,b) together with the open porosity on both scaffolds and a translucent appearance in the free of bioCaP scaffold, becoming whiter for the PLA-12CaP scaffold. The disposal of parallel lines of 0.8 mm thick with a separation between them of 0.4 mm perpendicularly alternating the direction of the processing lines between each overlapped layer is also shown (a-d). Moreover, the uniform distribution of open square-shaped pores of 0.4 x 0.4 mm forming a 3D cubic arrangement can also be observed.

The bonding configuration of PLA, PLA-1CaP, PLA-2CaP, and PLA-12CaP scaffolds was characterized by Raman spectroscopy and presented in Fig. 3. The characteristic spectrum of polylactic acid [49,50] was observed for the PLA scaffold (Fig. 3a) with leading strong bands registered, as expected, at: 872 cm^{-1} with an intense and sharp band attributed to C—COO stretching, 1769 cm^{-1} assigned to C = O

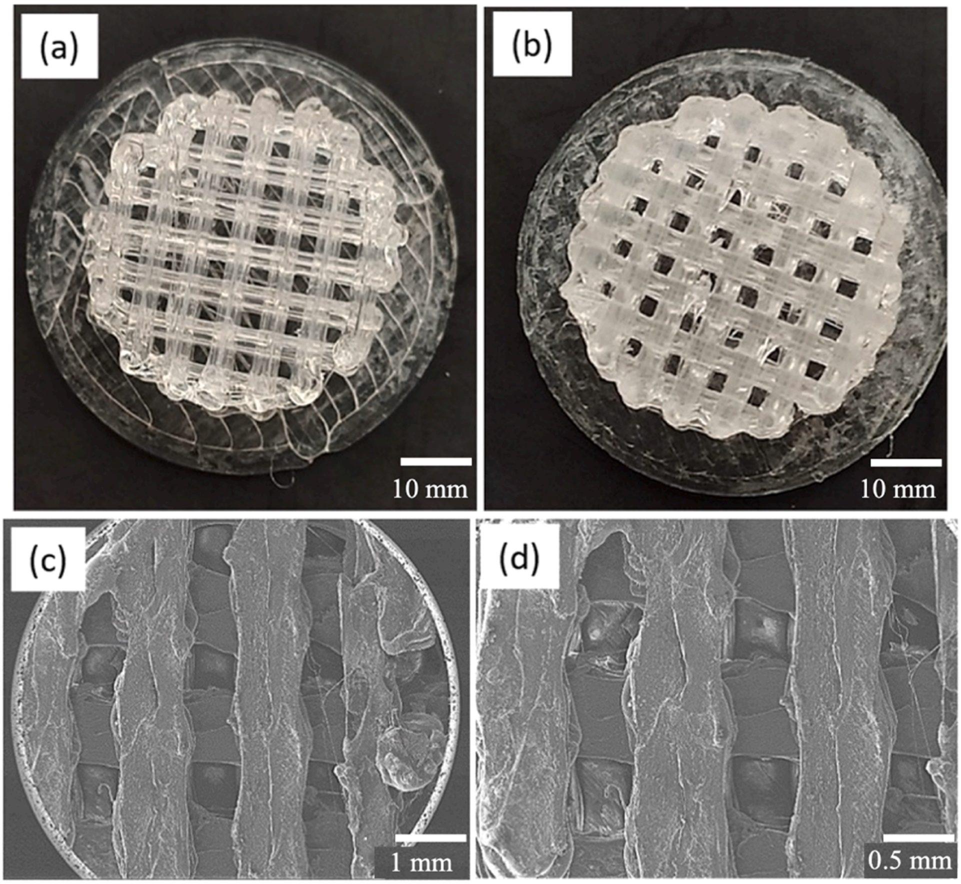

Fig. 2. Optical images x1 magnification of PLA with the porosity amplified for more detail (a) and the same for the PLA-12CaP scaffold (b). SEM micrographs of PLA-12CaP scaffolds at x25 (c) and x33 (d) magnifications.

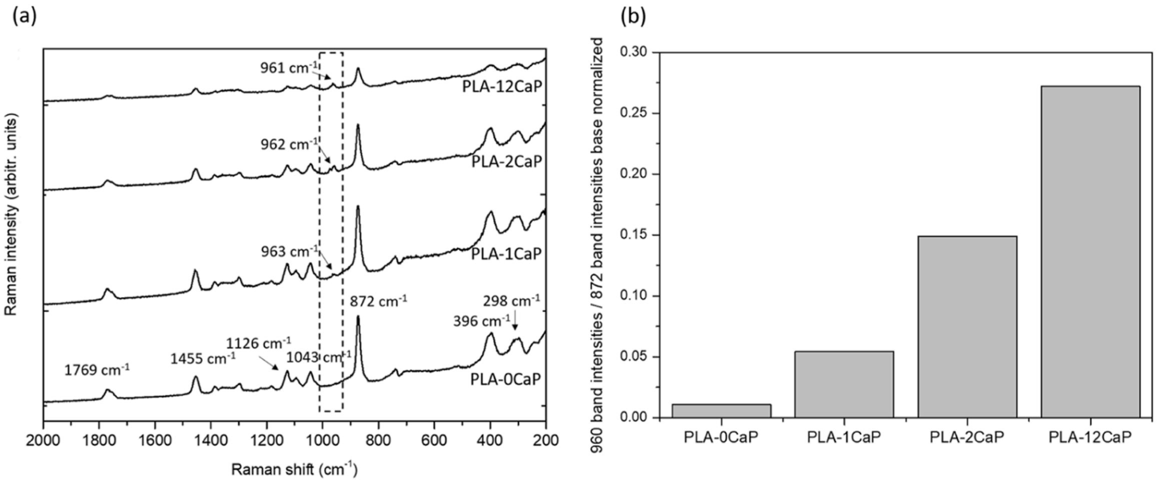

Fig. 3. Raman spectra of PLA, PLA-1CaP, PLA-2CaP, PLA-12CaP scaffolds where main strong bands characteristic for PLA at the region 2000–200 cm^{-1} and spectra region (1000–900 cm^{-1}) characteristic for main band of calcium phosphates (pointed square) are shown (a). Quantitative Raman evaluation to obtain the corresponding bioCaP: PLA ratio for the 3D printed scaffolds is also presented (b).

asymmetric stretching, 1455 cm^{-1} to asymmetric bending CH$_3$, 1126 cm^{-1} to asymmetric rocking CH$_3$, 1043 cm^{-1} attributed to skeletal stretching C—CH$_3$ and, finally, at 398 cm^{-1} and 298 cm^{-1} respectively assigned to bending CCO and COC. The Raman spectra obtained for PLA-1CaP, PLA-2CaP, and PLA-12CaP scaffolds (Fig. 3a) presented the same PLA characteristic bands together with, as expected, the band near 960 cm^{-1} attributed to PO$_4^{-3}$ symmetric stretching mode of calcium phosphates [51,52]. A quantitative evaluation from the Raman spectra was performed to obtain the bioCaP: PLA ratio for each of the 3D-printed scaffolds to continue with a more in-depth analysis. For it, Raman intensities of the band at 960 cm^{-1} attributed to calcium phosphates were divided between the corresponding ones for the band at 870 cm^{-1} assigned to polylactic acid, previous normalization with the spectra bases. As can be observed in Fig. 3b, the gradually increasing contribution of calcium phosphates in the 3D printed scaffolds was proven.

XDR determined the crystal structure of the 3D-printed scaffolds. In Fig. 4, diffraction patterns for PLA and PLA-2CaP scaffolds are presented. In the case of the 3D-printed PLA scaffold, a wide band between 2θ angle of 10° and 25° was observed, with a main broad peak at 14.99°, instead of the characteristic main peak expected for neat PLA diffractogram at 16.8° and a less intense one at 19.5° [53]. The broadband obtained is attributed in the literature to an intermediate order in the polymer chains between the amorphous and crystalline forms and, therefore, associated with the semi-crystalline nature of PLA [54–56]. When the 3D printed PLA-2CaP scaffold diffractogram was obtained, a weak band related to PLA appeared at 16.75° attributed to the α-form crystals at the plane (110)/(200), which implies a certain recrystallization of the polymer [53,57]. Moreover, sharp and intense diffraction peaks located at the characteristic region near 32° of hydroxyapatite (Ca$_5$(PO$_4$)$_3$(OH)) were detected, in particular the three peaks 31.77°, 32.17°, 32.88° respectively, corresponding to crystal planes of hexagonal hydroxyapatite (211), (112) and (300). Additionally, other diffraction peaks attributed to hydroxyapatite [51,58,59] were also measured at 10.81°, 25.84°, 28.89°, 34.05°, 39.79°, 46.64, 49.44° and 53.18° respectively attributed to (100), (002), (120), (202), (310), (222), (213) and (004). Finally, the diffraction peak observed at 28.02° is attributed to β-tricalcium phosphate (β-TCP) or whitlockite (214), according to Jang et al. (2014) [60]. The diffraction patterns confirmed, therefore, the increase in the degree of the crystallinity of the 3D printed scaffolds promoted by incorporating the bioceramic, including a certain

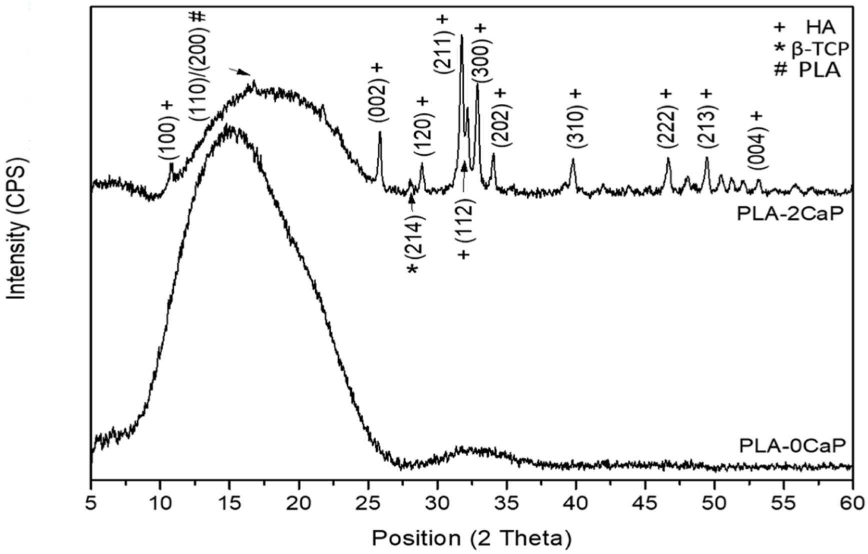

Fig. 4. XRD patterns of PLA and PLA-2CaP scaffolds in the range of positions between 5° and 60° where crystal planes attributed to polylactic acid (PLA), hydroxyapatite, and β-tricalcium phosphate/whitlockite are indicated.

re-crystallization of the 3D printed PLA.

Furthermore, printed samples were observed under SEM to evaluate the roughness of the implant's surface. Fig. 5 shows a clear difference in the surface topography of the scaffolds, being very smooth for the PLA group and becoming rougher in PLA-2-CaP and PLA12-CaP groups. A tendency to a rougher surface could be observed when increasing de wt. % of bioCaP, with apparent differences between PLA-2CaP and PLA-12CaP implants. Likewise, despite being successfully dispersed, bioCaP particles tend to form agglomerates, whose size and appearance increased parallel to the percentage of bioCaP. Thus, the bioceramic material changes the surface from smooth to rough, so the higher the concentration of bioCaP, the greater the roughness as it can be seen in Fig. 5, when magnified 400 times.

3.1.2. *Pore morphology*

The scaffolds present a highly interconnected square-shaped pore structure, as seen in SEM images, with open pores around their circumference, which favor cells and blood vessels growing toward the inner part of the implant. 3D composite scaffolds synthesized by Fused Deposition Modelling should be homogeneous, so we should be able to analyze the influence of different bioCaP proportions on porosity. The scaffolds' porosity was assessed for 2 samples of each group, obtaining a mean porosity value of 46±5%. The range of porosity measurements was between 40.30% and 51.38%. However, these differences seem to have been caused by the manufacturing process since there is no relationship between the results obtained and the amount of bioCaP.

The distribution of the pore size and strut thickness along the scaffolds was represented in Fig. 6. The mean values for all the groups of pore size and strut thickness were measured, resulting in 390±10μm and 390±50μm, respectively. However, if we analyze the results, it may be interesting to point out that mean values did not represent those pore size or strut thickness values that appear with greater frequency. So, the mode was calculated, and the results were included in Table 1. Differences to between the size of the 3D-printer's nozzle, and the strut thickness could be explained by rheological factors [61]. Since struts were thicker in the area where they overlap with others, they were narrower in the bridge areas (between two struts deposited perpendicularly). This consequently affected strut thickness and pore size measurements. Furthermore, micro-CT has certain limitations when measuring strut thickness, only providing measurements of the struts in these bridge areas. Furthermore, the dispersion of the bioCaP particles in the PLA struts along the longitudinal and cross-sectional axis was assessed. Micro-tomographic images showed the particles homogeneously dispersed superficially and inside of the struts, in line with what was observed in the images obtained by SEM (Fig. 7).

To obtain more data on the characteristics of pores, a study was conducted on pore interconnectivity. This helps denote the relations between two interlinked pores, indicating the level of connectivity of the porous structures. This attribute is vital to understanding the growth of cells. The connective porosity or accessible porosity consists of all the pores larger than the defined interconnective pore size. In this way, if the defined interconnection size was 0 (m), all the pores would be counted in the porosity, which means 100% effective porosity [43]. All the scaffolds were highly interconnected, with values equal to or higher than 90% of the pore connected to the outside environment through openings smaller than 162.56 μm. Very slight changes among groups can be observed in the percentage of pore accessibility until a pore size is less than 325.12 μm, with interconnectivity values still near 80%, as seen in Fig. 8. Regarding the minimum connection size of 596.05 μm, the PLA-2CaP group represented the lowest interconnection value (18%). Variations in pore accessibility seem to be related to the implants' porosity.

3.1.3. *Mechanical test*

Compressive strength was one of the most important scaffold properties, especially when these will be implanted in load-bearing sites. The mechanical properties of the scaffolds were tested in scaffolds ($n = 2$) from the different groups: PLA, PLA-1CaP, PLA-2CaP and PLA-12CaP. The calculated strength was taken at the end of the linear elasticity phase. The results of compressive strength and elastic modulus are shown in Table 2.

The compressive strength of PLA, PLA-1CaP, PLA-2CaP, and PLA-12CaP are collected in Table 2. As seen, adding bioCaP reinforces the composite's mechanical properties when a 2% bioCaP was used, but the PLA-12CaP presented a decrease in the compressive strength. Despite that, the strain-stress curves (Fig. 9) revealed a plastic material behavior in all the composites, showing the typically three different sections of porous materials: a linear elasticity phase, an intermediate plateau phase, and further densification, with stress increasing with the strain. A similar trend to that shown by the compressive strength can be observed in the elastic modulus, PLA-2CaP, the one with the highest values (444.44 MPa), which can even be compared with the one of the human skull bone (450 MPa) [62].

Furthermore, compressive strength was correlated with several pore

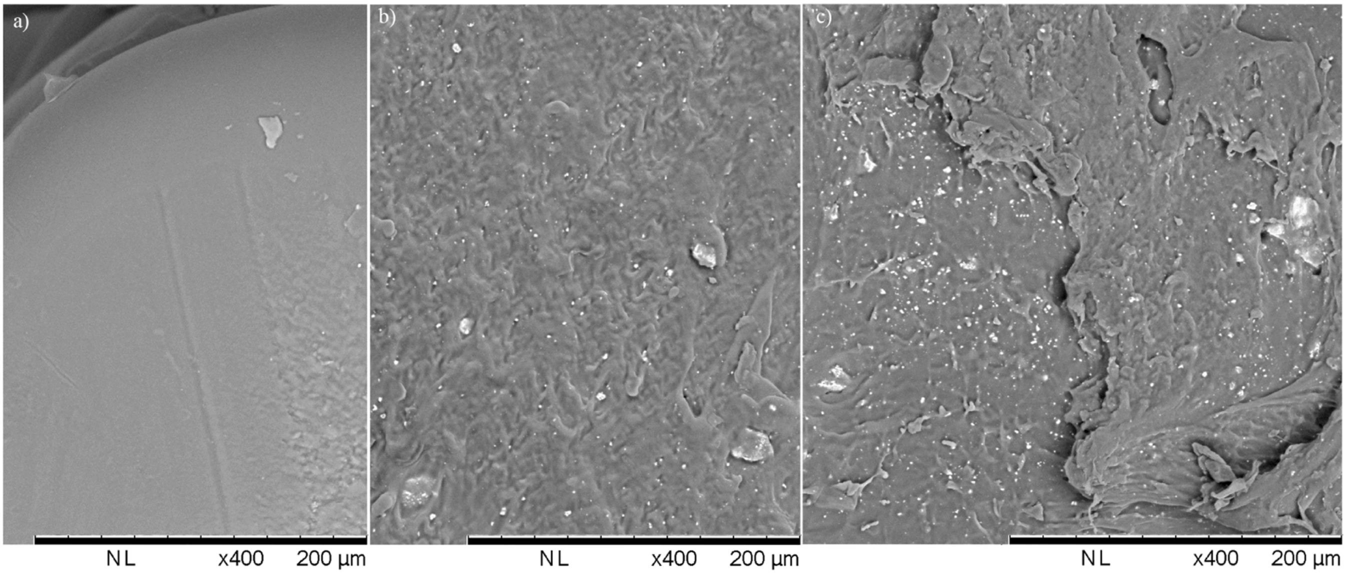

Fig. 5. The surface morphology of the scaffolds observed by SEM (x400 magnification): PLA (a), PLA-2CaP (b) and PLA-12CaP (c).

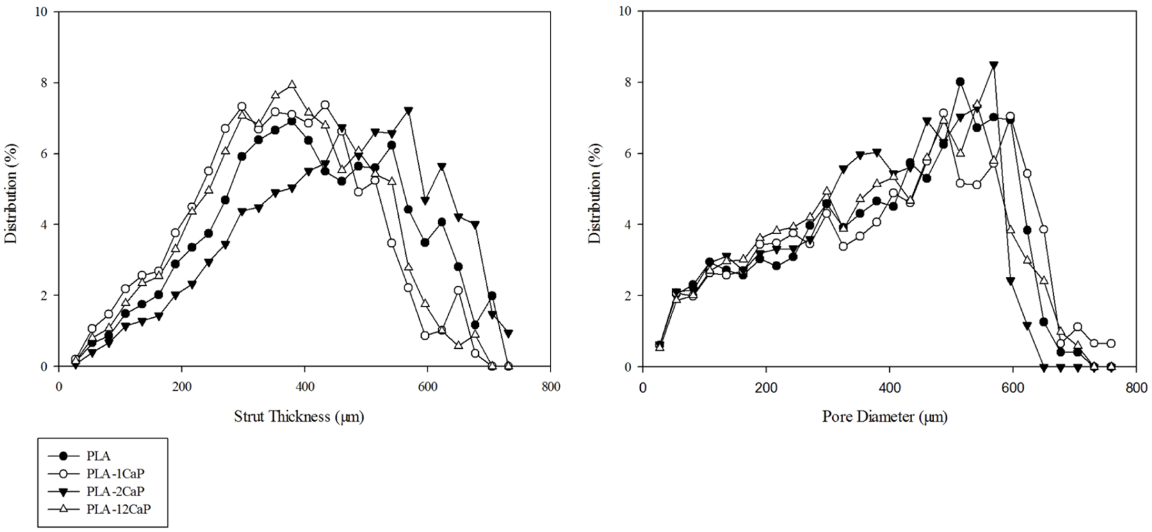

Fig. 6. Strut Thickness and Pore Size Distribution of 3D printed composite scaffolds.

Table 1
Pore morphology measurements in micro-CT. All parameters are represented as mean ± SD.

		PLA	PLA-1CaP	PLA-2CaP	PLA-12CaP
Open Porosity	%	44±6	50.8 ± 0.8	40.7 ± 0.5	48±2
Strut Thickness (mean)	µm	410 ±70	360±20	449.2 ± 0.9	370±20
Strut Thickness (mode)	µm	379.31	433.49	568.96	379.31
Pore Size (mean)	µm	400 ±10	410±20	377±4	388±1
Pore Size (mode)	µm	514.77	487.67	568.96	541.87

architectural characteristics of the scaffold (Table 3). And as expected, strong correlations were found between open porosity, surface area-to-volume ratio, and strut thickness, and compressive strength. Thus, the scaffolds' porosity may also influence their mechanical properties, so that by increasing open porosity or surface area to volume ratio, the compressive strength of the scaffold will decrease. In contrast, when increasing strut thickness, the compressive strength will increase, too.

3.1.4. *Wettability*

The water contact angle of the scaffolds was measured, and the results are given in Table 4. Each value is the average of contact angle measurements of 3 points. As results showed, the increasing content of bioCaP in the composites is not enough to modify the hydrophobic behavior of PLA. Contrary to what was expected, adding CaP increases the scaffolds' hydrophobicity.

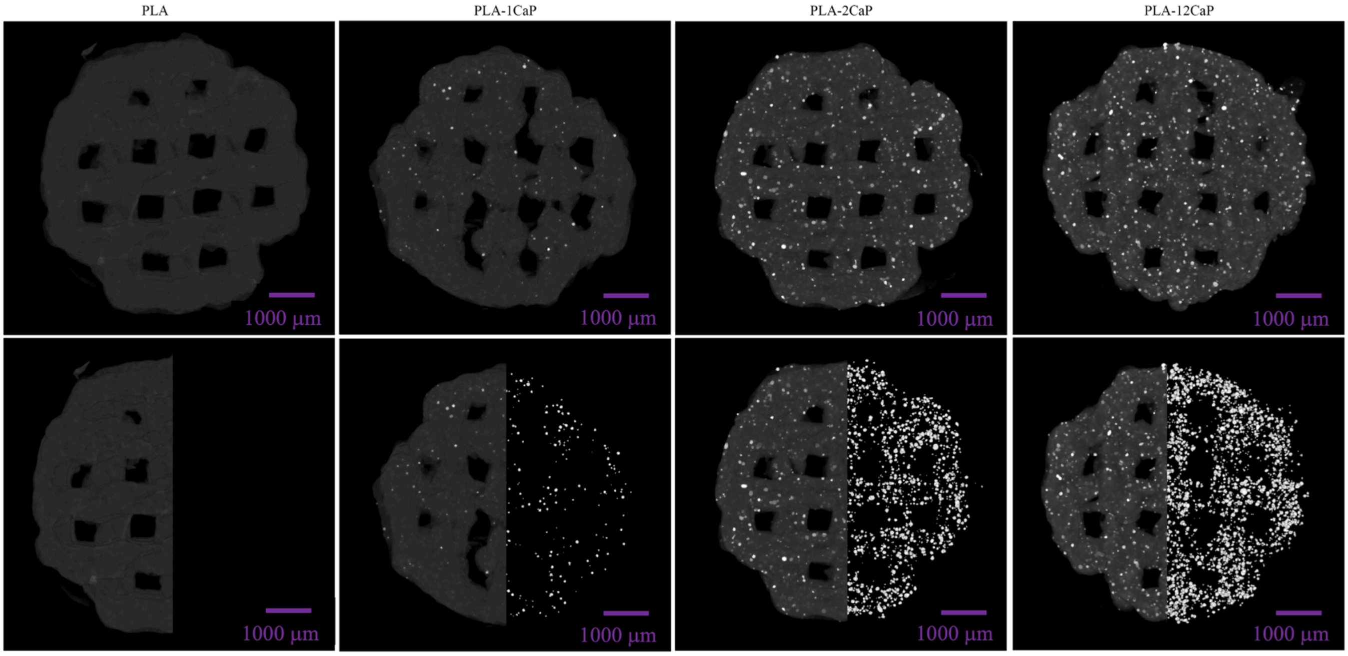

Fig. 7. Micro-CT reconstruction of 3D printed composite scaffolds, showing the dispersion of the different amounts of bioCaP (white dots) in different study groups.

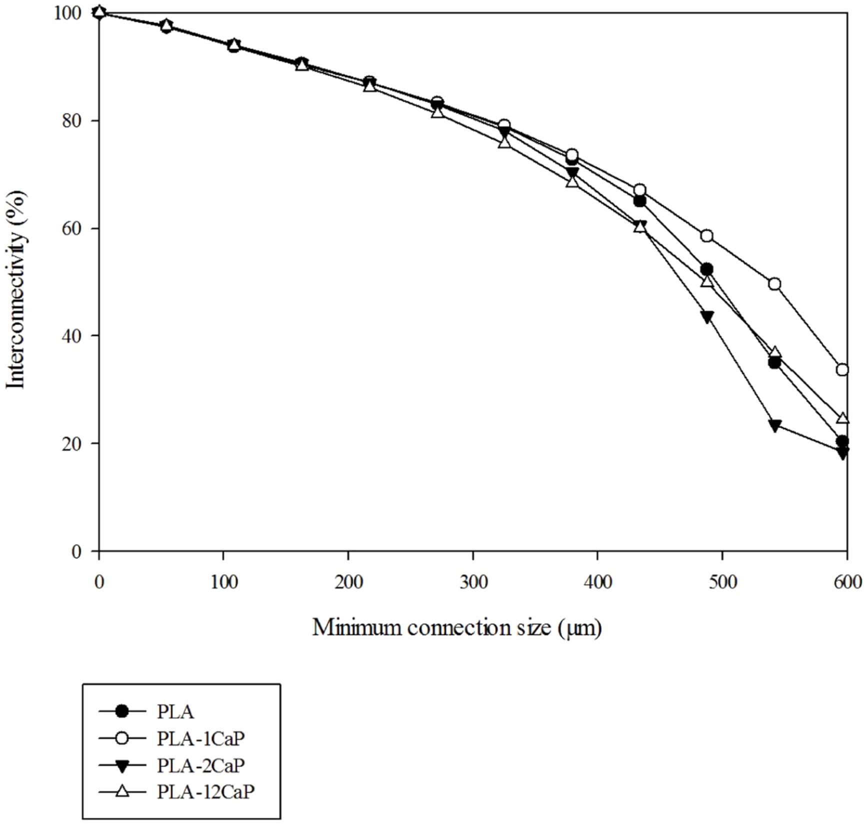

Fig. 8. Pore accessibility assessment in micro-CT.

Table 2
Mechanical Test Results. All parameters are represented as mean ± SD.

		PLA	PLA1CaP	PLA2CaP	PLA12CaP
Compressive Strength	MPa	44±5	37± 1	49±5	28±4
Elastic Modulus	MPa	350±50	278±4	410±40	250±30

3.2. Animal model

All in vivo experiments did not present complications, no adverse effects were observed after implantation, the animals recovered adequately, and the skin healed normally after the surgeries.

At the time of sacrifice, all the rabbits were healthy and did not present observable inflammatory reactions, furthermore, neurological reactions were absent.

During the necropsy, macroscopical examinations were conducted over all the implants, to ensure they had anchored adequately to the bone and fitted well in the defect. Furthermore, the absence of macroscopical signs of inflammation, hematoma or infection was confirmed. After the dissection of the implants' regions, only one rabbit presented adherences between the bottom of the implant and the duramater, but it could be extracted without complications.

3.3. Micro-CT

Micro-tomographic analysis was performed to evaluate the bone morphometric parameters mentioned above in the volume of interest: BV/TV, BS/BV, Tb.Th. and Tb.Pf.. Results are shown in Fig. 10. As it could be seen on it, there were no statistically significant differences for parameters referring to bone regeneration, such as BV/TV, which was higher for PLA (11.11 ± 3.26%) and PLA-12CaP (11.07 ± 4.33%) groups. However, there were no differences for bone surface-to-bone volume ratio (BS/BV), or trabecular thickness (Tb.Th.), which were very similar for all groups. PLA-12CaP group despite not being statistically significant, showed the highest trabecular values. Conversely, the same group showed statistically significant differences in values of the trabecular pattern factor (Tb.Pf) with PLA ($p = 0.00837$) and PLA-1CaP ($p = 0.00839$) groups. Representative images were included in Fig. 11.

3D images demonstrated good biocompatibility of the different scaffolds implanted in vivo. Most presented good integration with the host bone without signs of rejection. Strongly mineralized tissue ingrowth within the scaffolds could be observed, initially at the edge of the bone defect and then gradually filling inwards and toward the center. The same samples showed isolated bone growing in the inner part of the scaffold, probably occasioned by the migration of bone marrow cells because of the bleeding and clot formation during the surgical procedure. Bone tissue ingrowth occurred through the pores following its orientation, providing the scaffold with notable support to the host bone.

3.4. Histology

3.4.1. Qualitative histology

A rabbit model of calvarial defects was used to evaluate the osteogenic potential of rising concentrations of bioCaP mixed with PLA. Fig. 12 shows optical images of the histological slides. For the histological assessment, Lévai-Laczkó stained slides were subjected firstly to semi-quantitative evaluation techniques to quantify the inflammatory response, new blood vessel formation, and presence of fibrosis and fatty infiltrate to assess the local effects after implantation following UNE-EN ISO 10,993–6:2017 standards (Fig. 13).

Optical microscopy of the whole specimens was used to quantify cellular response by counting the number of polymorphonuclear cells, lymphocytes, plasma cells, macrophages, and giant cells per high-powered (400x) field (phf), focusing specifically on the biomaterials' contour (Fig. 14). They were scored from 0 to 5, denoting absence,

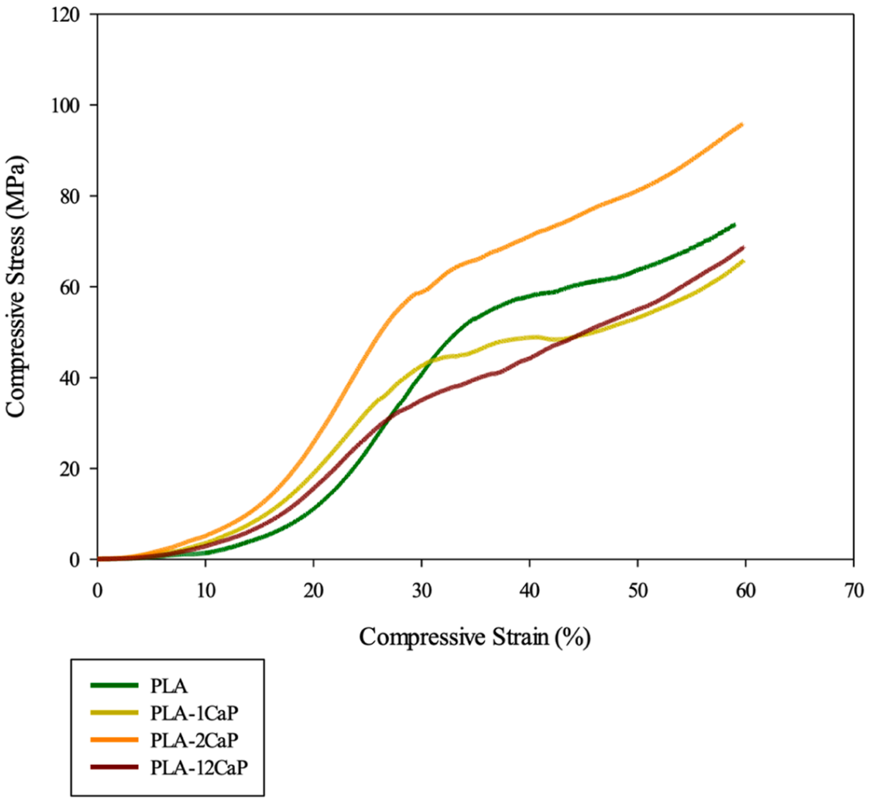

Fig. 9. Compressive Stress-Strain curves of 3D printed scaffolds.

Table 3
Correlation study between compressive strength and pore architectural characteristics of the fabricated scaffolds ($n = 8$, $*p < 0.05$).

Pearson's correlation coefficient	Open Porosity	Surface area-to-volume ratio	Strut Thickness
Compressive Strength	−0.79*	−0.80*	0.80*

Table 4
Contact angle measurements. All parameters are represented as mean ± SD.

	PLA	PLA1CaP	PLA2CaP	PLA12CaP
Contact Angle (Degrees)	100±10	100±20	130±20	120±20

presence of 1–5 cells/phf, presence of 5–10 cells/phf, heavy infiltrates or packed, respectively. Among the mentioned inflammatory cells, macrophages are the main ones found in the different specimens and are usually very close to the implant surface, with scores between 1 and 3. In addition, lymphocytes were identified in 4 samples. Three of them scored as 1, and the other one as 2. Finally, 1 to 5 giant cells/phf appeared in one of the samples. There were no findings of necrosis in any of the specimens.

Then, the rest of the parameters included in the UNE-EN ISO were evaluated. Firstly, fibrosis was the main finding in all the samples; narrow (1), to moderately thick (2), and even thick (3) bands were identified as filling the inner part of the implant and avoiding bone-implant contact, both inside the implant pores and with the bony surface of the defect. Likewise, fatty infiltrate was found in all the samples, which is usually associated with fibrosis. Among minimal amounts of fat (1), elongated and broad accumulations of fat cells were observed filling the space inside the implant. The neovascularization was also a phenomenon shared by almost all the specimens, which was semi-quantified as focal minimal capillary proliferation (1), groups of 4 to 7 capillaries (2) or broad bands (3) with supporting fibroblastic structures (Fig. 14). Besides, there was no evidence of traumatic necrosis or foreign debris.

Under the condition of this study, and in accordance with the provisions of the UNE-EN ISO 10,993–6:2017 standards, the tested samples were considered as non-irritant (PLA-1CaP and PLA-2CaP groups), and slight irritant (PLA-12CaP group) to the tissue as compared to PLA group. Furthermore, found statistically significant differences between the groups were found only for the quantification of macrophages between the PLA and PLA-12CaP groups ($p = 0.042$), the latter presenting high score values.

Another interesting aspect to highlight from the qualitative evaluation is the complete absence of bone growth in those points where the implants are not in contact with bone defect margins (Fig. 12), since the defects were slightly more significant than implants. This finding may demonstrate the ability of the implant to stimulate bone growth and the proposal of the defect as critical size. As it was explained in Micro-CT section, usually new bone was forming from the edge towards the center, being able to observe bridges' formation with ingrowth between scaffold struts (Fig. 12). Furthermore, isolated bone islands could be appreciated in the middle of the scaffolds, without connections with newly formed bone at the defect edges. All the scaffolds remained inside the defect, maintaining their structural integrity and without significant degradation observed.

3.4.2. *Histomorphometric analysis*

Histomorphometric parameters to evaluate Bone-to-Implant Contact (BIC), Implant Surface to Tissue Surface (IS/TS) and New Bone Surface to Tissue Surface (BS/TS), were assessed in the region of interest (ROI) for every single sample (Fig. 15). The analysis was performed after digital coloring of the images (Fig. 16), and the following results were obtained. Firstly, the percentage of implant surface inside the ROI was similar for all the groups without statistically significant p values, and mean values ranged between 41.52% ± 5.08 and 47.85% ± 8.78. This could indicate a similar degradation of the implants belonging to the

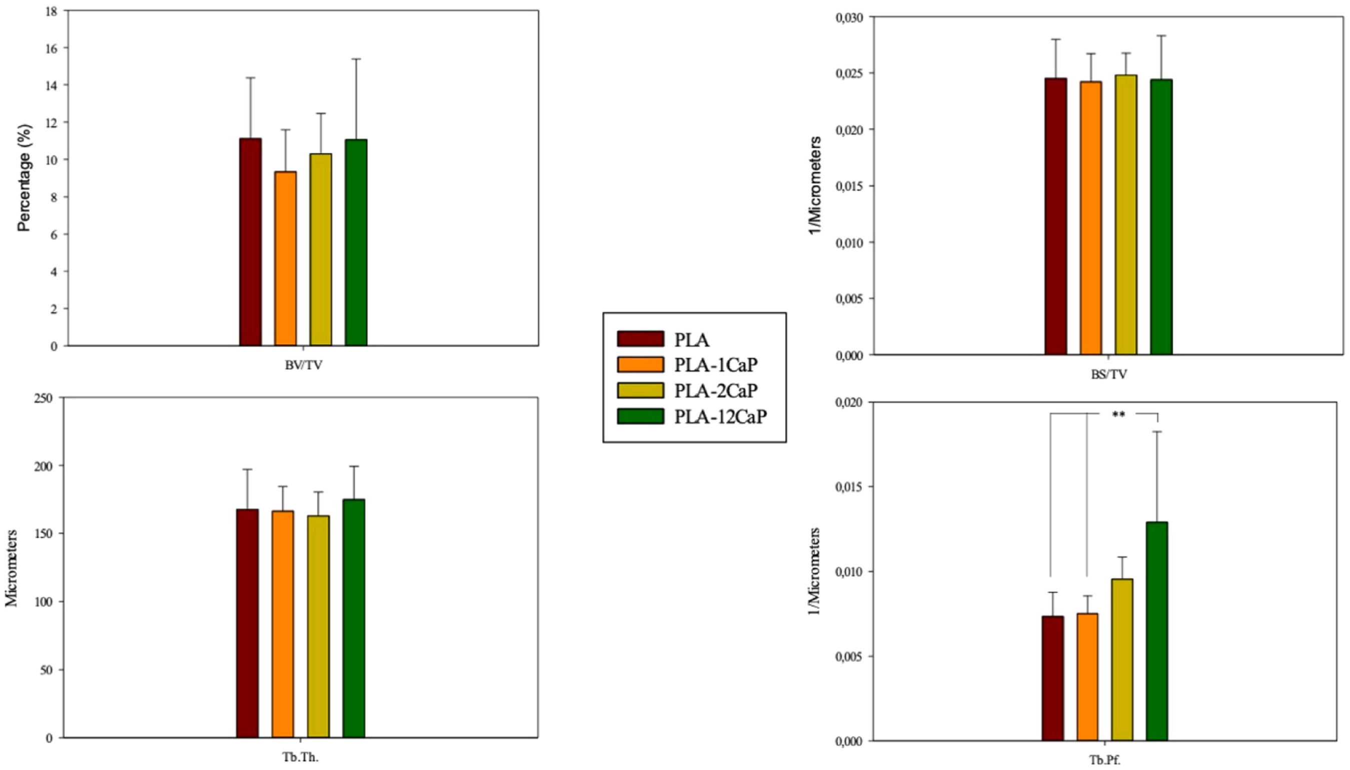

Fig. 10. Micro-CT histomorphometric measurements. BV/TV: Bone Volume/Tissue Volume, BS/BV: Bone Surface/Bone Volume, Tb.Th.: Trabecular Thickness and Tb.Pf.: Trabecular Pattern Factor. $^{**}p < 0.05$.

different groups, even though the variations that may exist due to the orientation of the histological section for the arrangement of the scaffolds' struts were considered, as it could be demonstrated in Fig. 12. Concerning BIC results, no statistical differences were found among the groups, however PLA group showed the highest BIC values, 7.90 ± 7.22, compared to PLA-12CaP group, which obtained the lowest ones, 3.78% ± 4.41, despite of the fact that it was the group with a higher percentage of calcium phosphate added. Finally, regarding to the percentage of new bone surface concerning to the tissue surface (BS/TS), the results in the assessed area showed that PLA group (18.23% ±5.70) is the one in which the greater amount of newly formed bone growing took place, followed by implanted scaffolds belonging to PLA-12CaP group (14.67% ± 5.26). In this case, statistically significant differences ($p < 0.031$) were found among PLA and PLA-2CaP groups (18.23% ±5.70 vs 11.69% ±3.06).

4. Discussion

The in vivo response of custom-designed 3D-printed composite PLA-bioCaP scaffolds with perpendicular patterning and open porosity (50%, pore size ~400 μm) was evaluated in a rabbit calvarial defect model. The proposed scaffolds displayed satisfactory physicochemical and mechanical properties. When implanted in vivo, no statistically significant differences were found after histologic and micro-tomographic new bone quantifications between composited and non-composited PLA groups, however the contribution of bioCaP in 12 wt.% promoted a positive influence in certain histomorphometric parameters, such as the connectivity of the trabecular bone.

According to Raman and SEM/XDR analysis results, bioCaP was successfully composited into the PLA matrix. So, PLA-bioCaP scaffolds were suggested as potential bone defect fillers. When synthesizing 3D-printed composites with bioceramic materials, it should be clear that the main mechanism of bioceramics' bioactivity is the partial dissolution of ionic products in vivo, elevating the concentration of calcium and phosphate ions, directly linked with the precipitation of biological apatite on the surface. This precipitation may incorporate various proteins and growth factors that promote cell attachment and function eventually leading to new bone formation. So, a greater surface area in contact with fluids will lead to faster dissolution rates [27]. Therefore, the improvement in osteogenic potential caused by the addition of the bioceramic materials will be closely related to the percentage of ceramic material exposed on the surface of the scaffold, either at the time of implantation or after the degradation of the polymeric matrix in this case. Since the composition and distribution of HA particles exposed on the surface are critical for cell-material interactions and osteoconductivity of the composite [63]. For this purpose, SEM analysis allows an exhaustive analysis of surface topography, identifying exposure points of bioCaP available to provide anchorage for cell spreading and adhesion. Possible control of point-exposed bioceramics in a composite enables the optimization of cell spreading and reduces the problem of deficient adhesion of bioceramics to PLA. However, although bioceramic particles can form a homogeneous suspension with the polymer, the amount of those particles that can appear on the surface may not reflect the average value of the bulk [63,64]. Furthermore, when working with biodegradable materials, factors related to polymer degradation products and its physicochemical and architectural changes must be carefully considered because of their effects on surrounding cells and tissues [64].

Furthermore, the apparition of bioCaP particles on the polymer's surface will have more implications on scaffolds' characteristics. As seen in SEM images, exposed particles increased surface roughness proportional to the amount of bioCaP added. A rougher surface has more area for cell to attach through proteins or integrins on the cell membrane and to proliferate better [63]. Our results are in agreement with those obtained by Corcione et al. [65], Wang et al. [66] or Wang et al. [67], where the addition of HA to a PLA matrix produces an increase in surface roughness. In addition, Akindoyo et al. [68] studied the dispersion of HA particles in a PLA matrix, successfully using a surface modifier

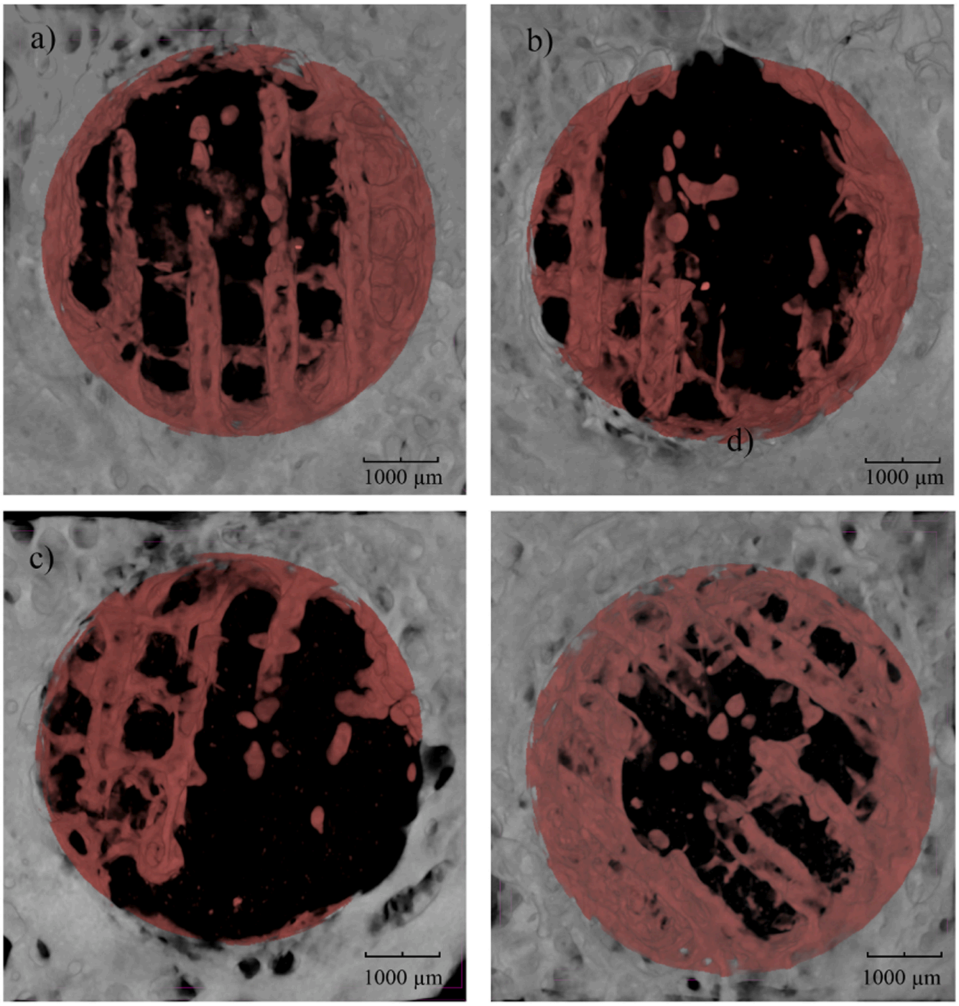

Fig. 11. Representative micro-CT images of the effect of composite scaffolds on bone regeneration at 12 weeks in calvarial rabbit defects. The measured volume of interest (VOI) was highlighted in red color. PLA a), PLA-1CaP b), PLA-2CaP c) and PLA-12CaP d).

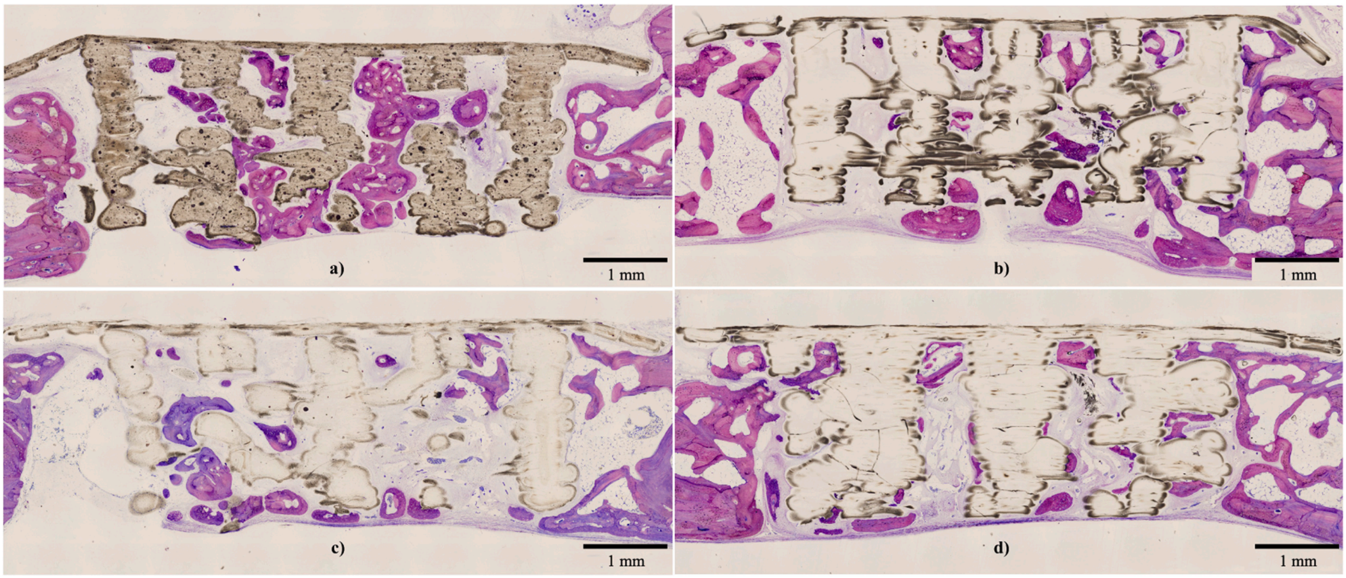

Fig. 12. Histological sections of the calvarial bone after 12 weeks of healing (Lévai-Laczkó staining). Sections clearly show typical findings of the samples. PLA-12CaP a), PLA-1CaP c), and PLA b) and d). The bone grows from the edges to the defects' center through the pore. Connective tissue filling the empty space. Absence of bone growing when the scaffold is not in contact with the margin of the defect. Struts with different thicknesses were present depending on where the section was performed.

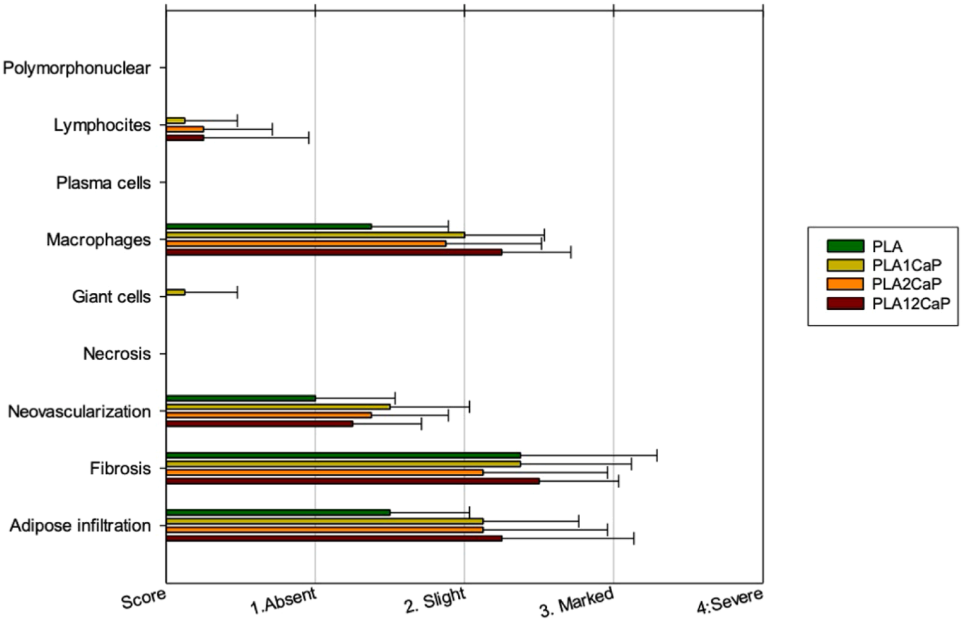

Fig. 13. UNE-EN ISO 10,993–6:2017 evaluation results summarized, classifying each parameter into different scores, being 0 equal to its absence and 1, 2, 3, and 4 equal to slight, moderate, marked, and severe presence, respectively.

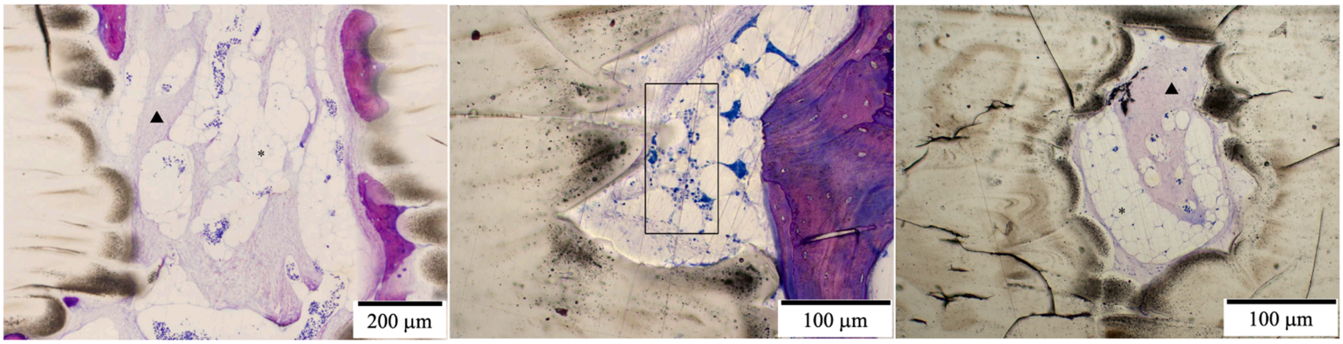

Fig. 14. Lévai-Laczkó stained slides demonstrated the findings described during the semi-quantitative evaluation. Fatty infiltrates could be observed (*), as well as fibrous band with different thicknesses (□), and macrophages were present near the composite material (black square).

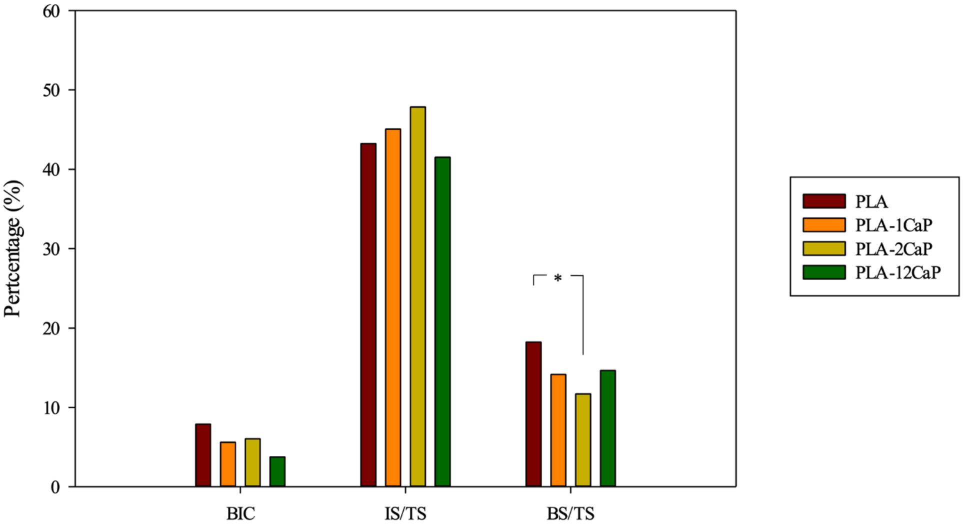

Fig. 15. Histomorphometric measurements. BIC: Bone-to-Implant Contact, IS/TS: Implant Surface to Tissue Surface, BS/TS: New Bone Surface to Tissue Surface. *$p < 0.05$.

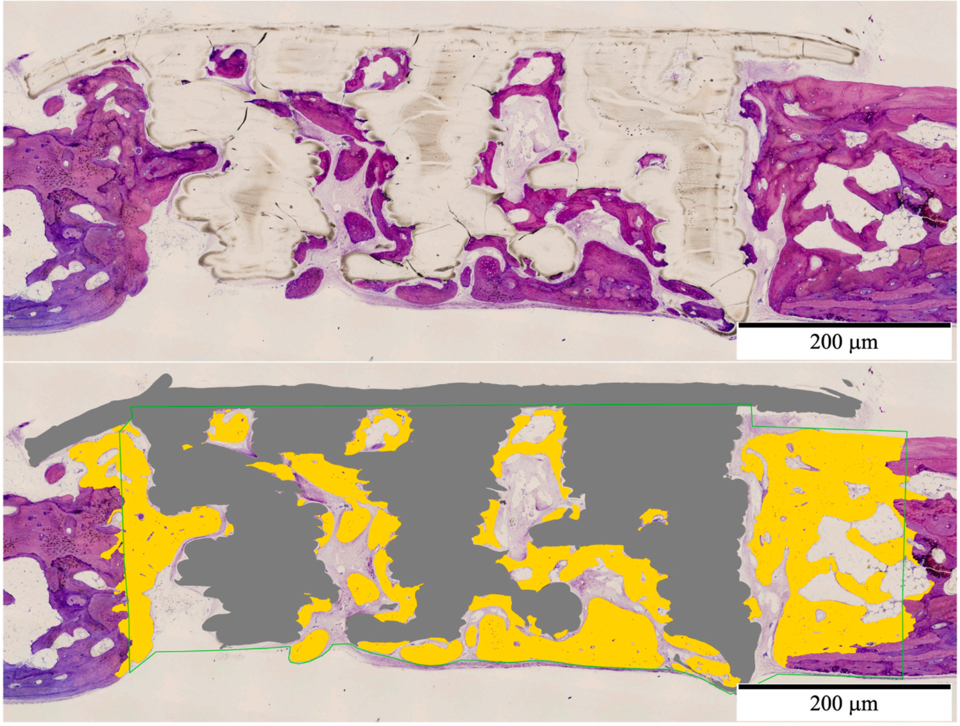

Fig. 16. Histological Lévai-Laczkó stained section belonging to PLA group, before and after being colored, indicating the analyzed Region of Interest, fitting the defect margins.

(Fabulase® 361), which notably improved the dispersion of the particles. Thus, avoiding one of the challenges often envisaged for PLA-HA composites, such as the agglomerations of HA in the PLA matrix, which can serve as points for stress concentrations leading to poor mechanical properties. Similarly, Zhang et al. [29] also obtained better dispersibility and fewer agglomerations after adding Dodecyl trimethoxy silane (WD-10) to modify the nano-HA added to the scaffolds. Another parameter that can influence the dispersion is the particles' size, the use of nano-hydroxyapatite instead of micro-sized one has been demonstrated to increase surface activity and dispersibility, as well as being less brittleness [66,67].

The main purpose of tissue engineering scaffolding is to provide a platform for cells involved in bone regeneration, being conductive for blood vessel invasion, cell migration, proliferation, differentiation, and communication. Cancellous bone structure is an ideal template for BTE scaffolds, it is spongy and has a porosity of 50–90%, so resembling its mimicry seems to be a reasonable idea for designing BTE scaffolds [66, 69]. In the present study, Micro-CT analysis measured the open porosity of highly interconnected 3D printed composite scaffolds. Results showed a range of measures between 40.301% and 51.38%, similar to those obtained in other studies that synthesized 3D printed PLA/bioceramic composites, ranging from 26.4% to 70% [4]. The variations in mean porosity values for the different groups seemed unrelated to the added percentage of bioCaP. These observations were in agreement with those obtained by Wang et al. [67], who observed that there was no correlation between the proportion of n-HA and the porosity of the printed sample, being only influenced by the filling rate and shape of the blueprint. However, Corcione et al. [65] observed a discrepancy between the theoretical scaffold porosity (50%) and the results obtained for the PLA group (39%) and PLA/sdHA (55%); according to the authors, these differences could be explained by the bigger thickness of the PLA struts and lower percentage of large pores, compared to PLA/sdHA ones. In addition, other important biomimetic porous structure parameters, such as pore size or pore accessibility, were measured. The mean pore size value for all the scaffolds in the present study was established at 390±10 µm.

At present, optimal pore size is still inconclusive since the change in experimental conditions can yield different results. On the one hand, microporosity improves surface area for protein adsorption, providing attachment points for osteoblasts. Nevertheless, tiny pores are non-conductive to cell migration and communications, leading to non-mineralized osteoid and fibrous tissue formation. Thus, 100 µm is considered the very minimum pore size. On the other hand, macroporosity promotes osteogenesis and vascularization. Although desirable pore sizes for cell growth, blood flux, and adequate mechanical properties could range between 100 and 1000 µm, pore size should vary between 200 and 600 µm, taking into account that sizes greater than 300 µm facilitate osteoblast proliferation and enhance vascularization [8, 69–72]. While pore size is essential, the interconnectivity and pore accessibility of the complicated network of pores are crucial to bone ingrowth. Pore accessibility gives the smallest pore constriction between the scaffold edge and any voxel within the scaffold pore space, demonstrating the inability of bone to grow into pores accessible through narrow constrictions [44]. Tiainen et al. [42] reported that scaffolds with average pore sizes close to 400 µm and high interconnectivity of 92% through connections as large as 200 µm will allow excellent permeability, sufficient tissue ingrowth, and vascularization for bone regeneration in TiO_2 scaffolds. The scaffolds proposed in the present work, according to pore accessibility results, have demonstrated high interconnectivity, with values equal to or higher than 90%. No similar studies with PLA-Bioceramic composites, including pore accessibility analysis, were found.

Mechanical properties are one of the main scaffold requirements for bone regeneration. PLA is a biopolymer with relatively high strength and modulus, which may vary depending on its molecular weight and degree of crystallinity [23]. Its compressive strength (2 - 39 MPa) is similar to that of natural bone (2–12 MPa) [67]. Micro- and nano-bioactive ceramic powders such as hydroxyapatite (HA) were incorporated to increase the printed PLA composites' mechanical strength and osseointegration properties. It has reported an improvement of the mechanical properties when the content of HA is lower than 15% [24,67,73]. Thus, balancing the ductility of PLA and the brittleness of CaP is a critical issue in regulating composites` mechanical properties [29]. However, Wang et al. [67] synthesized PLA-nanoHA scaffolds with a percentage from 10 to 50% of the bioceramic material, and results showed that the greater proportion of nanoHA, the lower the mechanical strength is. Similar results were obtained by other authors, such as Akindoyo et al. [68], who observed a reduction of tensile strength and flexible modulus when adding 5% and 20% of HA. Corcione et al. [65] appreciated a reduction of scaffold stiffness from 238 MPa to 124 MPa when adding 50% mesoporous micron-sized spherical HA power to a PLA matrix. These changes were attributed to morphological and microstructural differences between PLA and PLA-Bioceramic groups, such as surface roughness or overall porosity. So, the particles increased the available surface area. Still, contrary to what was expected, they did not act as reinforcement for the PLA matrix, even when the percentages were lower than 15% [65,73]. Nevertheless, when adding 10% wt or 30% wt of β-TCP to a PLA matrix, synthesized scaffolds demonstrated an increase of the mechanical properties, with an increase of the compressive modulus from 258±102 MPa in the PLA group to 349±51 MPa in the PLA-30%β-TCP group, achieving values similar to human skull bone (450 MPa) [62].

In the present study, compressive strength and elastic modulus of the scaffolds decreased notably when 12 wt.% of bioCaP was added to a PLA matrix, compared to PLA alone, 44 MPa vs 28 MPa, respectively. However, these results should be analyzed cautiously since, according to the obtained results, changes in the mechanical properties are highly related to variations in open porosity, surface area-to-volume, and strut thickness. Moreover, in general terms, it is stated that differences in mechanical properties of less than an order of magnitude cannot be considered. Both scaffolds PLA alone and PLA-12CaP would be considered at the same level at the mechanical point of view. Similar correlations among porosity and compressive strength were found by Tiainen et al. [42] for TiO_2 scaffolds ranging from 0.31 MPa to 3.14 MPa. Likewise, Chen et al. [74] suggested that changing the porosity can enhance the modulus of PLA-nHA scaffolds. It should be noted that even with the addition of CaP particles, scaffolds' mechanical properties were higher than that of pure HA (5.5 MPa) and human cancellous bone (5.5 MPa).

Surface wettability is another of the main parameters affecting the biological response to an implanted material, affecting protein adhesion to biomaterial surfaces [75]. Superhydrophilic (contact angle $< 2^\circ$) and superhydrophobic (contact angle $> 150^\circ$) polymer surfaces are not favorable for cell attachment and growth [76]. Regarding the wettability of the scaffolds, adding hydroxyapatite to synthesize a PLA/bioceramic composite is supposed to improve the hydrophilicity of the implant. Zhang et al. [29] obtained a reduction of the surface contact angle from 95.9° in the PLA group to 87.2° in PLA-30%nHA or 77.4° in PLA-50%nHA. However, in our study, the water contact angle results showed a greater hydrophobicity of the scaffolds as the percentage of hydroxyapatite increases. This can be explained by the Wenzel model, which states that as the roughness increases, the hydrophobicity or the hydrophilicity becomes stronger. A higher roughness of a surface will increase the surface area and, consequently, the interface between the liquid and the solid, exacerbating its surface properties. Thus, a hydrophilic surface will appear more hydrophilic, while a hydrophobic surface will appear more hydrophobic [77,78].

Traditionally, 2D histological and radiographical techniques were used to evaluate the osteointegration of tissue-engineered scaffolds. Despite being unable to provide all the data of a standard histological analysis, micro-CT has emerged as a fast and non-destructive tool to characterize and measure the 3D properties of scaffold or tissue-engineered constructs. This technique provides three-dimensional images of bone growing into scaffolds and allows its quantification in the hole volume of the defect region instead of only one slide. Furthermore, unlike bioceramic scaffolds, micro-CT allows easy detection of new bone formation in polymeric scaffolds due to its low attenuation [44,79,80]. Thus, it can be concluded that this technique cannot replace histology but can be used as a complementary evaluation method providing information of great interest. Likewise, the present manuscript found a strong correlation between micro-tomography and histomorphometry results ($p = 0.000000837$) when measuring bone regeneration.

The rabbit calvarial defects model was performed to evaluate the potential clinical application of 3D-printed PLA-bioCaP composite scaffolds. After the implantation, bone regeneration was assessed by micro-tomography and histomorphometry analysis. Micro-CT results demonstrated no differences among the four groups in BV/TV, BS/BV and Tb.Th; showing PLA-1CaP and PLA-2CaP groups the lowest values for the performed measurements. Likewise, regarding histomorphometric evaluations, statistically significant differences were found only for BS/TS, among PLA and PLA-2CaP groups. Therefore, contrary to what was expected, adding the already mentioned percentages of bioCaP did not seem to have a significant osteogenic effect. Similar studies were developed in rat calvarial defects. On the one hand, Gendviliene et al. [81] found no statistically significant differences between PLA and PLA-10%HA groups according to micro-CT and histological results; the amounts of regenerated bone were slightly higher when hydroxyapatite was added. On the other hand, Kwon et al. [62] fabricated 3D printed PLA scaffolds with increasing percentages of β-TCP (10% and 30%). In vivo trials they demonstrated, 12 weeks after implantation, that higher concentrations of the bioceramic were related with higher percentages of newly formed bone (around 10 and 25%, respectively). Likewise, other studies performed on rabbit's femoral diaphysis defects showed similar results. Wang et al. [67] implanted 3D-printed PLA composite scaffolds with 10% and 30% of nanoHA. It showed statistically significant differences among Pn0 and Pn30 groups when analyzing BV/TV in micro-CT, 1, 2, or 3 months after implantation. Finally, Wang et al. [66] implanted 3D-printed composite scaffolds with 50% of nanoHA and reported significative differences between PLA and PLA-nanoHA groups after 1,2 and 3 months.

The present manuscript, as described in the results' section, found statistically significant differences between PLA and PLA-1CaP groups and PLA-12CaP group when measuring Tb.Pf in micro-CT. This index describes the connectedness of individual trabeculae in a two-dimensional section, thus quantitatively describing the intertrabecular connectivity ratio. Then, results indicate that the addition of bioCaP possessed a positive and significant influence on the connectivity of the trabecular bone. The same trend was observed for Tb.Th., providing a higher trabecular thickness result for PLA-12CaP. However, no significant differences were found among the different groups when this parameter was microtomographically evaluated.

PLA is considered satisfactory regarding biocompatibility, although some cases of foreign body reactions and inflammatory reactions were reported [37,81,82]. From a qualitative histological analysis point of view, the implanted scaffolds in the present manuscript seemed biocompatible, showing slightly inflammatory effects, without signs of necrosis or the presence of foreign debris. Regarding the literature, different histological observations could be appreciated in papers referring to PLA and inflammation. On one side, Wang et al. [66] reported that no inflammatory cell aggregation was observed around the printed scaffolds, corroborating PLA's good biocompatibility. Likewise, Chen et al. [74] found no inflammatory response or formation of fibrous tissue near or inside the PLA/nHA scaffold. Zhang et al. [37] studied the cellular inflammatory reaction by hematology analysis, and no significant differences were detected between treated and non-treated groups. By the other side, Maia-Pinto et al. [83] described the presence of connective tissue interspersed with biomaterial and rare inflammatory cells in defects filled with neat PLA, and Gendviliene et al. [81] signaled the presence of lymphocytes, mainly in PLA group, and the presence of connective tissue with different thickness among the groups, which according to histological images seemed to appear between the scaffolds and the newly formed bone. Furthermore, Tcacencu et al. [84]

synthesized a composite structure based on a PLA porous disk thermally mounted on a apatite-wollastonite (AW, bioceramic material) disk. After implantation, AW, PLA, and AW/PLA groups demonstrated biocompatibility and were well integrated into the host tissue, with minimal evidence of inflammatory cell presence. However, regarding histological images belonging to AW/PLA group, it could be appreciated that bone was mainly in touch with the bioceramic material (AW), and PLA's surface was essentially in contact with fibrous tissue. As could be seen, the mentioned results agreed with those obtained in the present study.

The importance of using scaffolds in bone tissue engineering has increased in recent years, as it provides an alternative to autografts and allografts [37]. In this point, additive manufacturing techniques have provided essential advancements because they allow the customization of implants with complicated irregular geometries, precise internal and external architecture control, and high mechanical properties [29,37,65,83]. Among different available 3D printing techniques, extrusion-based ones have been demonstrated to be some of the most frequently utilized for the synthesis of PLA-Bioceramic composite scaffolds, specifically Fused Deposition Modelling (FDM) or Fused Filament Fabrication (FFF) [4]. This manuscript further studied the implications of the scaffold's morphological and compositional features and their effect on bone regeneration and implant biocompatibility. They are positioning 3D printing technologies as a mainstay for developing new bone grafts for bone tissue engineering in the future. Due to the wide range of possibilities, they offer regarding manufacturing parameters and customization, and the variety of biomaterials which allow working with.

Furthermore, ceramic materials have been successfully used for medical applications in the form of cements, coatings, scaffolds and paste, chiefly bioceramics such as calcium phosphates (hydroxyapatite, beta calcium phosphate, etc.) due to their resemblance to bone's mineral phase [26,27]. Chen et al. [74] reported some of the reasons for choosing HA as an inorganic filler, which could be extrapolated for the rest of calcium phosphate bioceramics, such as its role in favoring bone reconstruction, improving PLA's osteogenic, osteoconductive, and mechanical properties, and buffering the acidic by-products produced during PLA's degradation, therefore blocking the unfavorable cellular environment. Thus, HA included in composite scaffolds will prolong PLA degradation, reducing the acidity and increasing osteoconductivity of the scaffolds [81]. In our case, the use of fish-derived bioapatite also aims to improve PLA's physical and biological properties while at the same time pursuing the revalorization of fishing by-products. Furthermore, this bioceramic material proved its feasibility in synthesizing composite material by mixing it with a polymeric matrix, showing mild or absent inflammation after being implanted in vivo.

The calvarial bone defect model has been extensively used, mainly in rodent models, when studying bone healing and regeneration processes. Due to its easy performance, there is no need for external fixation, and bone healing can be assessed using micro-CT and histology easily. However, it does not allow the evaluation of the scaffold under physiological mechanical loads [81].

To summarize, the low osteogenic capabilities of the fabricated PLA-bioCaP composite implants could be explained as a mixture of the many reasons discussed above. Firstly, the inflammatory effects of PLA and acidic by-products of its degradation can lead to an unfavorable environment for bone growth. Besides, the amount of bioCaP added to the scaffolds may not be enough to provide the already described buffering effect and modify the polymeric material's hydrophobic surface. It was further proved that the high HA content (50%) could effectively reduce the acidity of the surrounding microenvironment [29]. Likewise, a low percentage of bioCaP will lead to a low exposure of the bioceramic particles calcium and phosphate available ions for bone regeneration. Gendviliene et al. [81] also noticed that an increase in HA concentration can provide better osteoconductive potential and be associated with higher levels of new bone formation.

The beneficial effect of pure PLA scaffolds on bone growth observed in some of the samples included in the present work could be explained by the capabilities of scaffold architecture and surface topography over PLA degradation. Likewise, in those samples where no bioCaP was added, the hydrophobicity of the implants could lead to lower degradation values and consequently to lower acidification of the environment, improving bone regeneration.

The amount of bioCaP incorporated in the present work is within the ranges of bioceramics combined with PLA in other studies [4]. Besides, authors such as Wang et al. [67] reported that contributions of bioceramics in values <15 wt.% has been proven to ensure a higher compressive strength of the PLA-based composite scaffold, as well as maintaining their biological properties. Anyway, a higher contribution in bioCaP could be indeed incorporated by 3D printing methodologies in future investigations. This should be performed to enhance the bioCaP amount in the composite scaffolds to obtain a higher exposure to the surface of the bioCaP particles and improve their osteogenic capabilities, as well as improvements in the surface's hydrophobicity, probably related to the presence of slight inflammation signs, and a detailed analysis on the degradation, to characterize the degradation rate and the environment's acidification.

One widely used alternative to improve the scaffolds' osteogenic potential by adding different substances to functionalize the scaffolds. Successful results by using these substances and comparing the obtained results with non-functionalized groups, were described by many authors as Alonso-Fernandez et al. [4] reported in their systematic review. Some substances included in the mentioned review are dental pulp stem cells, bone marrow stem cells, bone morphogenetic proteins, enhanced bone marrow or osteoblastoma cell lines. They all have demonstrated an improvement in the osteogenic potential of the synthesized scaffolds. Another possible strategy to achieve this goal could be the biomimetic mineralization of the scaffolds as described by Maia-Pinto et al. [83], who based on the importance of the surface characteristics of biomaterials for successful medica applications, utilized calcium phosphate coatings to improve scaffold's bioactivity and osteoconductivity. Furthermore, to improve tissue regeneration, they also incorporated biological mediators to the implants, specifically growth factors, such as recombinant human bone morphogenetic protein-2 (rhBMP-2), due to its great osteoinductive potential.

5. Conclusion

Additive manufacturing techniques allow the customization of 3D-printed scaffolds that perfectly fit patients' defect morphology. In the present manuscript, 3D-printed composite PLA-based scaffolds with perpendicular patterning, open porosity (50%, pore size ~400 μm), high interconnectivity (>90%) and composition (bioCaP up to 12% wt.) were manufactured by Fused Deposition Modelling and displayed satisfactory mechanical properties, biocompatibility and osteoconductivity being a suitable alternative for repairing bone defects in animals or humans. the scaffolds' hydrophilicity, nor did adding marine bioCaP to the polymeric matrix used here did not improve the scaffolds' hydrophilicity or mechanical resistance. However, despite their hydrophobicity, the structures demonstrated suitable characteristics to support bone regeneration, promoting it at similar levels as the PLA. The highest tested contribution in bioCaP promoted a significant favorable influence in certain histomorphometry parameters, such as the connectivity of the trabecular bone. However, the scaffold's osteogenic potential was not proved for the tested compositions. Further research is required to optimize the composition for osteogenic potential.

Funding sources

This study was funded by the GRC support program from Xunta de Galicia (GRC ED431C 2021/19 and ED431C 2021/49) and the UE project IBEROS+ (0072_IBEROS_MAIS_1_E), which was financed by the POCTEP 2021-2027 FEDER program.

CRediT authorship contribution statement

Iván Alonso Fernández: Writing – original draft, Resources, Project administration, Methodology, Investigation, Formal analysis, Data curation, Conceptualization. **Håvard Jostein Haugen:** Writing – review & editing, Visualization, Validation, Supervision. **Liebert Parreiras Nogueira:** Software, Methodology, Formal analysis. **Miriam López Álvarez:** Writing – review & editing, Resources, Investigation, Data curation. **Pío González:** Supervision, Resources, Methodology, Funding acquisition. **Mónica López Peña:** Supervision, Project administration, Methodology. **Antonio González Cantalapiedra:** Supervision, Methodology, Funding acquisition. **Fernando Muñoz Guzón:** Visualization, Supervision, Project administration, Methodology, Funding acquisition, Conceptualization.

Declaration of competing interest

The authors declare that they have no known competing financial interests or personal relationships that could have appeared to influence the work reported in this paper.

Acknowledgments

I.A. acknowledges the XUNTA de Galicia for his pre-doctoral contract (Ref. ED481A 2021/137) from Galician Government Consellería de Cultura, Educación e Universidades.

References

[1] Tumedei, Savadori, D. Fabbro, Synthetic blocks for bone regeneration: a systematic review and meta-analysis, IJMS 20 (2019) 4221, https://doi.org/10.3390/ijms20174221.

[2] L. Roseti, V. Parisi, M. Petretta, C. Cavallo, G. Desando, I. Bartolotti, B. Grigolo, Scaffolds for Bone Tissue Engineering: state of the art and new perspectives, Mater. Sci. Eng.: C 78 (2017) 1246–1262, https://doi.org/10.1016/j.msec.2017.05.017.

[3] D. Tang, R.S. Tare, L.-Y. Yang, D.F. Williams, K.-L. Ou, R.O.C. Oreffo, Biofabrication of bone tissue: approaches, challenges and translation for bone regeneration, Biomaterials 83 (2016) 363–382, https://doi.org/10.1016/j.biomaterials.2016.01.024.

[4] I. Alonso-Fernández, H.J. Haugen, M. López-Peña, A. González-Cantalapiedra, F. Muñoz, Use of 3D-printed polylactic acid/bioceramic composite scaffolds for bone tissue engineering in preclinical in vivo studies: a systematic review, Acta Biomater. 168 (2023) 1–21, https://doi.org/10.1016/j.actbio.2023.07.013.

[5] S. Hosseinpour, M. Ghazizadeh Ahsaie, M. Rezai Rad, M.T. Baghani, S. R. Motamedian, A. Khojasteh, Application of selected scaffolds for bone tissue engineering: a systematic review, Oral Maxillofac. Surg. 21 (2017) 109–129, https://doi.org/10.1007/s10006-017-0608-3.

[6] M. Majidinia, A. Sadeghpour, B. Yousefi, The roles of signaling pathways in bone repair and regeneration, J. Cell Physiol. 233 (2018) 2937–2948, https://doi.org/10.1002/jcp.26042.

[7] Y. Li, S.K. Chen, L. Li, L. Qin, X.L. Wang, Y.X. Lai, Bone defect animal models for testing efficacy of bone substitute biomaterials, J. Orthop. Translat. 3 (2015) 95–104, https://doi.org/10.1016/j.jot.2015.05.002.

[8] H.J. Haugen, S.P. Lyngstadaas, F. Rossi, G. Perale, Bone grafts: which is the ideal biomaterial? J. Clin. Periodontol. 46 (2019) 92–102, https://doi.org/10.1111/jcpe.13058.

[9] S. Bose, S. Vahabzadeh, A. Bandyopadhyay, Bone tissue engineering using 3D printing, Mater. Today 16 (2013) 496–504, https://doi.org/10.1016/j.mattod.2013.11.017.

[10] L. Polo-Corrales, M. Latorre-Esteves, J.E. Ramirez-Vick, Scaffold design for bone regeneration, J. Nanosci. Nanotech. 14 (2014) 15–56, https://doi.org/10.1166/jnn.2014.9127.

[11] F. Liu, Y. Liu, X. Li, X. Wang, D. Li, S. Chung, C. Chen, I.-S. Lee, Osteogenesis of 3D printed macro-pore size biphasic calcium phosphate scaffold in rabbit calvaria, J. Biomater. Appl. 33 (2019) 1168–1177, https://doi.org/10.1177/0885328218825177.

[12] G. Fernandez de Grado, L. Keller, Y. Idoux-Gillet, Q. Wagner, A.-M. Musset, N. Benkirane-Jessel, F. Bornert, D. Offner, Bone substitutes: a review of their characteristics, clinical use, and perspectives for large bone defects management, J. Tissue Eng. 9 (2018) 204173141877681, https://doi.org/10.1177/2041731418776819.

[13] S. Hammouche, D. Hammouche, M. McNicholas, Biodegradable bone regeneration synthetic scaffolds: in tissue engineering, CSCR 7 (2012) 134–142, https://doi.org/10.2174/157488812799219018.

[14] H. Shao, A. Liu, X. Ke, M. Sun, Y. He, X. Yang, J. Fu, L. Zhang, G. Yang, Y. Liu, S. Xu, Z. Gou, 3D robocasting magnesium-doped wollastonite/TCP bioceramic scaffolds with improved bone regeneration capacity in critical sized calvarial defects, J. Mater. Chem. B 5 (2017) 2941–2951, https://doi.org/10.1039/C7TB00217C.

[15] J. Yun, J. Lee, C.W. Ha, S.J. Park, S. Kim, K. Koo, Y. Seol, Y. Lee, The effect of 3-D printed polylactic acid scaffold with and without hyaluronic acid on bone regeneration, J. Periodontol. (2022) 1–11, https://doi.org/10.1002/jper.21-0428.

[16] H. Pae, J. Kang, J. Cha, J. Lee, J. Paik, U. Jung, B. Kim, S. Choi, 3D-printed polycaprolactone scaffold mixed with β-tricalcium phosphate as a bone regenerative material in rabbit calvarial defects, J. Biomed. Mater. Res. 107 (2019) 1254–1263, https://doi.org/10.1002/jbm.b.34218.

[17] G. Brunello, S. Sivolella, R. Meneghello, L. Ferroni, C. Gardin, A. Piattelli, B. Zavan, E. Bressan, Powder-based 3D printing for bone tissue engineering, Biotechnol. Adv. 34 (2016) 740–753, https://doi.org/10.1016/j.biotechadv.2016.03.009.

[18] X. Du, S. Fu, Y. Zhu, 3D printing of ceramic-based scaffolds for bone tissue engineering: an overview, J. Mater. Chem. B 6 (2018) 4397–4412, https://doi.org/10.1039/C8TB00677F.

[19] J.-W. Kim, B.-E. Yang, S.-J. Hong, H.-G. Choi, S.-J. Byeon, H.-K. Lim, S.-M. Chung, J.-H. Lee, S.-H. Byun, Bone regeneration capability of 3D printed ceramic scaffolds, IJMS 21 (2020) 4837, https://doi.org/10.3390/ijms21144837.

[20] M.S. Singhvi, S.S. Zinjarde, D.V. Gokhale, Polylactic acid: synthesis and biomedical applications, J. Appl. Microbiol. 127 (2019) 1612–1626, https://doi.org/10.1111/jam.14290.

[21] D.W. Hutmacher, M. Sittinger, M.V. Risbud, Scaffold-based tissue engineering: rationale for computer-aided design and solid free-form fabrication systems, Trend. Biotechnol. 22 (2004) 354–362, https://doi.org/10.1016/j.tibtech.2004.05.005.

[22] J.M. Latimer, S. Maekawa, Y. Yao, D.T. Wu, M. Chen, W.V. Giannobile, Regenerative medicine technologies to treat dental, oral, and craniofacial defects, Front. Bioeng. Biotechnol. 9 (2021) 704048, https://doi.org/10.3389/fbioe.2021.704048.

[23] V. DeStefano, S. Khan, A. Tabada, Applications of PLA in modern medicine, Eng. Regenerat. 1 (2020) 76–87, https://doi.org/10.1016/j.engreg.2020.08.002.

[24] E.H. Tümer, H.Y. Erbil, Extrusion-based 3D printing applications of PLA composites: a review, Coatings 11 (2021) 390, https://doi.org/10.3390/coatings11040390.

[25] A.A. Al-allaq, J.S. Kashan, A review: in vivo studies of bioceramics as bone substitute materials, Nano Select. 4 (2023) 123–144, https://doi.org/10.1002/nano.202200222.

[26] G. Brunello, S. Panda, L. Schiavon, S. Sivolella, L. Biasetto, M.D. Fabbro, The impact of bioceramic scaffolds on bone regeneration in preclinical in vivo studies: a systematic review, Mater. (Basel) 13 (2020) 1–26, https://doi.org/10.3390/ma13071500.

[27] N. Eliaz, N. Metoki, Calcium phosphate bioceramics: a review of their history, structure, properties, coating technologies and biomedical applications, Mater. (Basel) 10 (2017) 334, https://doi.org/10.3390/ma10040334.

[28] Q. Yao, J.G.L. Cosme, T. Xu, J.M. Miszuk, P.H.S. Picciani, H. Fong, H. Sun, Three dimensional electrospun PCL/PLA blend nanofibrous scaffolds with significantly improved stem cells osteogenic differentiation and cranial bone formation, Biomaterials 115 (2017) 115–127, https://doi.org/10.1016/j.biomaterials.2016.11.018.

[29] B. Zhang, L. Wang, P. Song, X. Pei, H. Sun, L. Wu, C. Zhou, K. Wang, Y. Fan, X. Zhang, 3D printed bone tissue regenerative PLA/HA scaffolds with comprehensive performance optimizations, Mater. Des. 201 (2021), https://doi.org/10.1016/j.matdes.2021.109490.

[30] M. Alksne, M. Kalvaityte, E. Simoliunas, I. Rinkunaite, I. Gendviliene, J. Locs, V. Rutkunas, V. Bukelskiene, In vitro comparison of 3D printed polylactic acid/hydroxyapatite and polylactic acid/bioglass composite scaffolds: insights into materials for bone regeneration, J. Mech. Behav. Biomed. Mater. 104 (2020) 103641, https://doi.org/10.1016/j.jmbbm.2020.103641.

[31] A. Smieszek, K. Marycz, K. Szustakiewicz, B. Kryszak, S. Targonska, K. Zawisza, A. Watras, R.J. Wiglusz, New approach to modification of poly (l-lactic acid) with nano-hydroxyapatite improving functionality of human adipose-derived stromal cells (hASCs) through increased viability and enhanced mitochondrial activity, Mater. Sci. Eng. C Mater. Biol. Appl. 98 (2019) 213–226, https://doi.org/10.1016/j.msec.2018.12.099.

[32] S. Sultan, N. Thomas, M. Varghese, Y. Dalvi, S. Joy, S. Hall, A.P. Mathew, The design of 3D-printed polylactic acid–bioglass composite scaffold: a potential implant material for bone tissue engineering, Molecules 27 (2022) 7214, https://doi.org/10.3390/molecules27217214.

[33] N. Soehling, S. Al Zoghool, E. Schaetzlein, J. Neijhoft, K.M.C. Oliveira, L. Leppik, U. Ritz, E. Doersam, J. Frank, I. Marzi, A. Blaeser, D. Henrich, In vitro evaluation of a 20% bioglass-containing 3D printable PLA composite for bone tissue engineering, Int. J. Bioprint. 8 (2022) 65–81, https://doi.org/10.18063/ijb.v8i4.602.

[34] S. Gnanamani Sankaravel, R.B. Syed, V. Manivachakan, In vitro and mechanical characterization of PLA/egg shell biocomposite scaffold manufactured using fused deposition modeling technology for tissue engineering applications, Polym. Compos. 43 (2022) 173–186, https://doi.org/10.1002/pc.26365.

[35] E.H. Backes, L. de N. Pires, H.S. Selistre-de-Araujo, L.C. Costa, F.R. Passador, L. A. Pessan, Development and characterization of printablePLA/beta-TCPbioactive composites for bone tissue applications, J. Appl. Polym. Sci. 138 (2021), https://doi.org/10.1002/app.49759.

[36] M. López-Álvarez, E. Vigo, C. Rodríguez-Valencia, V. Outeiriño-Iglesias, P. González, J. Serra, In vivo evaluation of shark teeth-derived bioapatites, Clin. Oral Impl. Res. 28 (2017) e91–e100, https://doi.org/10.1111/clr.12934.

[37] H. Zhang, X. Mao, Z. Du, W. Jiang, X. Han, D. Zhao, D. Han, Q. Li, Three dimensional printed macroporous polylactic acid/hydroxyapatite composite scaffolds for promoting bone formation in a critical-size rat calvarial defect model,

Sci. Technol. Adv. Mater. 17 (2016) 136–148, https://doi.org/10.1080/14686996.2016.1145532.

[38] M. García-González, F.M. Muñoz Guzón, A. González-Cantalapiedra, P. M. González-Fernández, R. Otero Pérez, J.A. Serra Rodríguez, Application of shark teeth–derived bioapatites as a bone substitute in veterinary orthopedics. Preliminary clinical trial in dogs and cats, Front. Vet. Sci. 7 (2020) 574017, https://doi.org/10.3389/fvets.2020.574017.

[39] M. López-Álvarez, S. Pérez-Davila, C. Rodríguez-Valencia, P. González, J. Serra, The improved biological response of shark tooth bioapatites in a comparative in vitro study with synthetic and bovine bone grafts, Biomed. Mater. 11 (2016) 035011, https://doi.org/10.1088/1748-6041/11/3/035011.

[40] J. Rojas-Lozano, P. Días-Rodriguez, P. Barreiro, E. López-Senraa, C. Rodríguez-Valencia, M. López-Álvarez, M. Landín, P. González, P. Serra, Desarrollo de nuevos filamentos para impresión 3D basados en cerámicas bioinspiradoras, Materiales Compuestos 3 (2019) 65–69.

[41] L.A. Feldkamp, L.C. Davis, J.W. Kress, Practical cone-beam algorithm, J. Opt. Soc. Am. A 1 (1984) 612, https://doi.org/10.1364/JOSAA.1.000612.

[42] H. Tiainen, S.P. Lyngstadaas, J.E. Ellingsen, H.J. Haugen, Ultra-porous titanium oxide scaffold with high compressive strength, J. Mater. Sci.: Mater. Med. 21 (2010) 2783–2792, https://doi.org/10.1007/s10856-010-4142-1.

[43] H.-B. Wu, H.J. Haugen, E. Wintermantel, Supercritical CO_2 in injection molding can produce open porous polyurethane scaffolds – a parameter study, J. Cellul. Plast. 48 (2012) 141–159, https://doi.org/10.1177/0021955X11432970.

[44] A. Jones, C. Arns, A. Sheppard, D. Hutmacher, B. Milthorpe, M. Knackstedt, Assessment of bone ingrowth into porous biomaterials using MICRO-CT, Biomaterials 28 (2007) 2491–2504, https://doi.org/10.1016/j.biomaterials.2007.01.046.

[45] A. Klemm, H. Tiainen, Highly porous Sr-doped TiO2 ceramics maintain compressive strength after grain boundary corrosion, J. Eur. Ceram. Soc. 41 (2021) 5721–5727, https://doi.org/10.1016/j.jeurceramsoc.2021.04.059.

[46] N. Percie du Sert, V. Hurst, A. Ahluwalia, S. Alam, M.T. Avey, M. Baker, W. J. Browne, A. Clark, I.C. Cuthill, U. Dirnagl, M. Emerson, P. Garner, S.T. Holgate, D.W. Howells, N.A. Karp, S.E. Lazic, K. Lidster, C.J. MacCallum, M. Macleod, E. J. Pearl, O.H. Petersen, F. Rawle, P. Reynolds, K. Rooney, E.S. Sena, S. D. Silberberg, T. Steckler, H. Würbel, The ARRIVE guidelines 2.0: updated guidelines for reporting animal research, PLoS Biol. 18 (2020) e3000410, https://doi.org/10.1371/journal.pbio.3000410.

[47] N. Otsu, A threshold selection method from gray-level histograms, IEEE Trans. Syst., Man, Cybern. 9 (1979) 62–66, https://doi.org/10.1109/TSMC.1979.4310076.

[48] K. Donath, The diagnostic value of the new method for the study of undecalcified bones and teeth with attached soft tissue, (Säge-Schliff, (sawing and grinding) technique), Pathol. - Res. Pract. 179 (1985) 631–633, https://doi.org/10.1016/S0344-0338(85)80209-0.

[49] G. Kister, G. Cassanas, M. Vert, Effects of morphology, conformation and configuration on the IR and Raman spectra of various poly(lactic acid)s, Polym. (Guildf.) 39 (1998) 267–273, https://doi.org/10.1016/S0032-3861(97)00229-2.

[50] M.G. Gandolfi, F. Zamparini, M. Degli Esposti, F. Chiellini, C. Aparicio, F. Fava, P. Fabbri, P. Taddei, C. Prati, Polylactic acid-based porous scaffolds doped with calcium silicate and dicalcium phosphate dihydrate designed for biomedical application, Mater. Sci. Eng.: C 82 (2018) 163–181, https://doi.org/10.1016/j.msec.2017.08.040.

[51] H. Aguiar, S. Chiussi, M. López-Álvarez, P. González, J. Serra, Structural characterization of bioceramics and mineralized tissues based on Raman and XRD techniques, Ceram. Int. 44 (2018) 495–504, https://doi.org/10.1016/j.ceramint.2017.09.203.

[52] S. Koutsopoulos, Synthesis and characterization of hydroxyapatite crystals: a review study on the analytical methods, J. Biomed. Mater. Res. 62 (2002) 600–612, https://doi.org/10.1002/jbm.10280.

[53] S. Nanaki, P. Barmpalexis, A. Iatrou, E. Christodoulou, M. Kostoglou, D. Bikiaris, Risperidone controlled release microspheres based on poly(lactic acid)-poly (propylene adipate) novel polymer blends appropriate for long acting injectable formulations, Pharmaceutics 10 (2018) 130, https://doi.org/10.3390/pharmaceutics10030130.

[54] S. Mondal, T.P. Nguyen, V.H. Pham, G. Hoang, P. Manivasagan, M.H. Kim, S. Y. Nam, J. Oh, Hydroxyapatite nano bioceramics optimized 3D printed poly lactic acid scaffold for bone tissue engineering application, Ceram. Int. 46 (2020) 3443–3455, https://doi.org/10.1016/j.ceramint.2019.10.057.

[55] M. Tanase-Opedal, E. Espinosa, A. Rodríguez, G. Chinga-Carrasco, Lignin: a biopolymer from forestry biomass for biocomposites and 3D printing, Mater. (Basel) 12 (2019) 3006, https://doi.org/10.3390/ma12183006.

[56] M.M. Rahman, S. Afrin, P. Haque, Md.M. Islam, M.S. Islam, Md.A. Gafur, Preparation and characterization of jute cellulose crystals-reinforced poly(L-lactic acid) biocomposite for biomedical applications, Int. J. Chem. Eng. 2014 (2014) 1–7, https://doi.org/10.1155/2014/842147.

[57] M.A. Nazeer, O.C. Onder, I. Sevgili, E. Yilgor, I.H. Kavakli, I. Yilgor, 3D printed poly(lactic acid) scaffolds modified with chitosan and hydroxyapatite for bone repair applications, Mater. Today Commun. 25 (2020) 101515, https://doi.org/10.1016/j.mtcomm.2020.101515.

[58] I. Fernandez-Cervantes, M.A. Morales, R. Agustin-Serrano, M. Cardenas-Garcia, P. V. Perez-Luna, B.L. Arroyo-Reyes, A. Maldonado-Garcia, Polylactic acid/sodium alginate/hydroxyapatite composite scaffolds with trabecular tissue morphology designed by a bone remodeling model using 3D printing, J. Mater. Sci. 54 (2019) 9478–9496, https://doi.org/10.1007/s10853-019-03537-1.

[59] J.M. Hughes, M. Cameron, J. Rakovan, Structural variations in natural F,OH, and CL apatites, Am. Mineralog. 74 (1989) 870–876.

[60] H.L. Jang, K. Jin, J. Lee, Y. Kim, S.H. Nahm, K.S. Hong, K.T. Nam, Revisiting whitlockite, the second most abundant biomineral in bone: nanocrystal synthesis in physiologically relevant conditions and biocompatibility evaluation, ACS Nano 8 (2014) 634–641, https://doi.org/10.1021/nn405246h.

[61] L. González-Rodríguez, S. Pérez-Davila, R. Lama, M. López-Álvarez, J. Serra, B. Novoa, A. Figueras, P. González, 3D printing of PLA:CaP:GO scaffolds for bone tissue applications, RSC Adv. 13 (2023) 15947–15959, https://doi.org/10.1039/D3RA00981E.

[62] D.Y. Kwon, J.H. Park, S.H. Jang, J.Y. Park, J.W. Jang, B.H. Min, W.-D. Kim, H. B. Lee, J. Lee, M.S. Kim, Bone regeneration by means of a three-dimensional printed scaffold in a rat cranial defect, J. Tissue Eng. Regen. Med. 12 (2018) 516–528, https://doi.org/10.1002/term.2532.

[63] L. Cai, A.S. Guinn, S. Wang, Exposed hydroxyapatite particles on the surface of photo-crosslinked nanocomposites for promoting MC3T3 cell proliferation and differentiation, Acta Biomater. 7 (2011) 2185–2199, https://doi.org/10.1016/j.actbio.2011.01.034.

[64] S.C. Rizzi, D.J. Heath, A.G.A. Coombes, N. Bock, M. Textor, S. Downes, Biodegradable polymer/hydroxyapatite composites: surface analysis and initial attachment of human osteoblasts, J. Biomed. Mater. Res. 55 (2001) 445–669, https://doi.org/10.1002/1097-4636(20010615)55:4<475::AID-JBM1039>3.0.CO;2-Q.

[65] C. Esposito Corcione, F. Gervaso, F. Scalera, S.K. Padmanabhan, M. Madaghiele, F. Montagna, A. Sannino, A. Licciulli, A. Maffezzoli, Highly loaded hydroxyapatite microsphere/PLA porous scaffolds obtained by fused deposition modelling, Ceram. Int. 45 (2019) 2803–2810, https://doi.org/10.1016/j.ceramint.2018.07.297.

[66] W. Wang, B. Zhang, L. Zhao, M. Li, Y. Han, L. Wang, Z. Zhang, J. Li, C. Zhou, L. Liu, Fabrication and properties of PLA/nano-HA composite scaffolds with balanced mechanical properties and biological functions for bone tissue engineering application, Nanotechnol. Rev. 10 (2021) 1359–1373, https://doi.org/10.1515/ntrev-2021-0083.

[67] W. Wang, B. Zhang, M. Li, J. Li, C. Zhang, Y. Han, L. Wang, K. Wang, C. Zhou, L. Liu, Y. Fan, X. Zhang, 3D printing of PLA/n-HA composite scaffolds with customized mechanical properties and biological functions for bone tissue engineering, Composit. Part B-Eng. 224 (2021), https://doi.org/10.1016/j.compositesb.2021.109192.

[68] J.O. Akindoyo, M.D.H. Beg, S. Ghazali, H.P. Heim, M. Feldmann, Effects of surface modification on dispersion, mechanical, thermal and dynamic mechanical properties of injection molded PLA-hydroxyapatite composites, Composit. Part A: Appl. Sci. Manufact. 103 (2017) 96–105, https://doi.org/10.1016/j.compositesa.2017.09.013.

[69] G. Zhu, T. Zhang, M. Chen, K. Yao, X. Huang, B. Zhang, Y. Li, J. Liu, Y. Wang, Z. Zhao, Bone physiological microenvironment and healing mechanism: basis for future bone-tissue engineering scaffolds, Bioact. Mater. 6 (2021) 4110–4140, https://doi.org/10.1016/j.bioactmat.2021.03.043.

[70] N. Abbasi, S. Hamlet, R.M. Love, N.-T. Nguyen, Porous scaffolds for bone regeneration, J. Sci.: Adv. Mater. Dev. 5 (2020) 1–9, https://doi.org/10.1016/j.jsamd.2020.01.007.

[71] A.R. Amini, C.T. Laurencin, S.P. Nukavarapu, Bone Tissue Engineering: Recent Advances and Challenges, 2013.

[72] S.G. Pedrero, P. Llamas-Sillero, J. Serrano-López, A multidisciplinary journey towards bone tissue engineering, Mater. (Basel) 14 (2021) 4896, https://doi.org/10.3390/ma14174896.

[73] M. Milazzo, N. Contessi Negrini, S. Scialla, B. Marelli, S. Farè, S. Danti, M. J. Buehler, Additive manufacturing approaches for hydroxyapatite-reinforced composites, Adv. Funct. Mater. 29 (2019) 1903055, https://doi.org/10.1002/adfm.201903055.

[74] X. Chen, C. Gao, J. Jiang, Y. Wu, P. Zhu, G. Chen, 3D printed porous PLA/nHA composite scaffolds with enhanced osteogenesis and osteoconductivity in vivo for bone regeneration, Biomed. Mater. 14 (2019), https://doi.org/10.1088/1748-605X/ab388d.

[75] B. Majhy, P. Priyadarshini, A.K. Sen, Effect of surface energy and roughness on cell adhesion and growth – facile surface modification for enhanced cell culture, RSC Adv. 11 (2021) 15467–15476, https://doi.org/10.1039/D1RA02402G.

[76] L.-C. Xu, C.A. Siedlecki, Effects of surface wettability and contact time on protein adhesion to biomaterial surfaces, Biomaterials 28 (2007) 3273–3283, https://doi.org/10.1016/j.biomaterials.2007.03.032.

[77] J. Wang, Y. Wu, Y. Cao, G. Li, Y. Liao, Influence of surface roughness on contact angle hysteresis and spreading work, Colloid. Polym. Sci. 298 (2020) 1107–1112, https://doi.org/10.1007/s00396-020-04680-x.

[78] R.N. Wenzel, Resistance of solid surfaces to wetting by water, Ind. Eng. Chem. 28 (1936) 988–994, https://doi.org/10.1021/ie50320a024.

[79] A.C. Jones, B. Milthorpe, H. Averdunk, A. Limaye, T.J. Senden, A. Sakellariou, A. P. Sheppard, R.M. Sok, M.A. Knackstedt, A. Brandwood, D. Rohner, D. W. Hutmacher, Analysis of 3D bone ingrowth into polymer scaffolds via micro-computed tomography imaging, Biomaterials 25 (2004) 4947–4954, https://doi.org/10.1016/j.biomaterials.2004.01.047.

[80] F. Peyrin, Evaluation of bone scaffolds by micro-CT, Osteoporos. Int. 22 (2011) 2043–2048, https://doi.org/10.1007/s00198-011-1609-y.

[81] I. Gendviliene, E. Simoliunas, M. Alksne, S. Dibart, E. Jasiuniene, V. Cicenas, R. Jacobs, V. Bukelskiene, V. Rutkunas, Effect of extracellular matrix and dental pulp stem cells on bone regeneration with 3D printed PLA/HA composite scaffolds, Eur. Cell Mater. 41 (2021) 204–215, https://doi.org/10.22203/eCM.v041a15.

[82] K. Athanasiou, Sterilization, toxicity, biocompatibility and clinical applications of polylactic acid/polyglycolic acid copolymers, Biomaterials 17 (1996) 93–102, https://doi.org/10.1016/0142-9612(96)85754-1.

[83] M.O.C. Maia-Pinto, A.C.B. Brochado, B.N. Teixeira, S.C. Sartoretto, M.J. Uzeda, A. T.N.N. Alves, G.G. Alves, M.D. Calasans-Maia, R.M.S.M. Thiré, R.M.S.M. Thire, R. M.S.M. Thiré, Biomimetic mineralization on 3D printed PLA scaffolds: on the response of human primary osteoblasts spheroids and in vivo implantation, Polym. (Basel) 13 (2021), https://doi.org/10.3390/polym13010074.

[84] I. Tcacencu, N. Rodrigues, N. Alharbi, M. Benning, S. Toumpaniari, E. Mancuso, M. Marshall, O. Bretcanu, M. Birch, A. McCaskie, K. Dalgarno, Osseointegration of porous apatite-wollastonite and poly(lactic acid) composite structures created using 3D printing techniques, Mater. Sci. Eng. C-Mater. Biolog. Applic. 90 (2018) 1–7, https://doi.org/10.1016/j.msec.2018.04.022.